

# Performance of the MICE diagnostic systems

5

A.N. Other et al.

## Abstract

This paper will describe:

- The detectors as we have it installed in the MICE Hall at November 2017
- The performances of the detectors and the PID
- The absorbers model(s) and their validation
- The track matching
- The detector alignment

10

Reference to the published papers. Target: JINST volume.

Table 1: Status of the paper

Contribution	Plots	Text
TOF	First version	First version
Cherenkov	No	Introduction
KL	Yes	First version
EMR	First version	Two sections
Tracker	Some	Introduction
PID	No	No
Track matching	First version	first version
Detector alignment	Yes	First version
Magnets	No	No
Target model	No	No
Absorber model	No	Introduction

## Contents

15	<b>1 Introduction</b>	2
	<b>2 Time-of-Flight Detectors</b>	3
	2.1 Introduction . . . . .	3
	2.2 TEMPORARY - Plots . . . . .	6
	2.3 Calibration Method . . . . .	6
20	2.4 Reconstruction . . . . .	12
	2.5 Performance . . . . .	12
	<b>3 Cherenkov Detectors</b>	13
	3.1 Introduction . . . . .	13
	3.2 Performance . . . . .	13

25	<b>4 KLOE-Light Calorimeter</b>	<b>13</b>
	4.1 Introduction . . . . .	13
	4.2 Performance . . . . .	14
	<b>5 Electron Muon Ranger</b>	<b>17</b>
30	5.1 Introduction . . . . .	17
	5.2 Performance . . . . .	18
	<b>6 The Trackers</b>	<b>25</b>
	6.1 Introduction . . . . .	25
	6.2 Tracker Performance and Reconstruction . . . . .	26
	6.3 Tracker Efficiency Evolution . . . . .	26
35	<b>7 PID</b>	<b>27</b>
	7.1 Introduction . . . . .	27
	7.2 Performance of the PID . . . . .	27
	<b>8 Track Matching</b>	<b>27</b>
40	8.1 Global reconstruction . . . . .	27
	8.2 Beam based magnet alignment . . . . .	39
	<b>9 Beam-based detector alignment</b>	<b>39</b>
45	9.1 Introduction . . . . .	40
	9.2 Analysis method . . . . .	41
	9.3 Alignment of a data sample . . . . .	45
	9.4 Propagation . . . . .	46
	<b>10 Magnets and Beam Optics</b>	<b>51</b>
	10.1 Introduction . . . . .	51
	10.2 Beam based magnet alignment . . . . .	51
	10.3 Beam line optics . . . . .	51
50	<b>11 Absorber</b>	<b>51</b>
	11.1 Absorber vessel body . . . . .	52
	11.2 Windows . . . . .	52
	11.3 Validation of the absorber model in MAUS . . . . .	54
	11.4 refs . . . . .	54
55	<b>12 Conclusions</b>	<b>54</b>

## 1 Introduction

To include:

- Motivation
- Outline of the experiment

60 **2 Time-of-Flight Detectors**

List of figures

- PMT charge correlation PMT0 vs PMT1 - maybe, if relevant
- *TW calibration of one channel*
- *Slab DT before TW correction and after - single pixel.*
- 65 • *Residual TW*
- T0 correction for 1 channel - electron peak fit
- *(?) Slab DT mean and sigma for all pixels after calibration*
  - *depends on whether we are comfortable with showing it*
- 70 • *Overall slab DT*
- Space-point creation efficiency per pixel/slab
  - *this is tricky, the only inefficiency comes from time mismatch*
  - *it can point to a fact that some slabs/pixels have something wrong with them*
  - *it is not measure of performance per se*
- Particle detection efficiency
  - *don't know how to extract from the data, ideally pixel map for each TOF*

75 *Issues:*

- should we use word “counter” or “slab”?

## 2.1 Introduction

Three time-of-flight detectors (TOF0, TOF1, TOF2) have been built and installed at RAL in 2008 and 2009  
80 to measure the position and the time of crossing particles. TOF0 and TOF1 [1], [2], [3] are placed upstream of the cooling channel, and TOF2 [4] is downstream of the channel, mounted in front of the KL, as shown in Fig. ???. The time of flight between two TOF stations provides particle identification information and can also be used for momentum measurement. TOF1 served most of the time also as an experimental trigger. They have smoothly operated during the so-called Step I and Step IV [5], [6] running periods of the MICE experiment  
85 and were essential for all the measurements done.

The good performances of the TOF detectors, over an extended period of time, has enabled the MICE experiment to characterize fully its muon beams during Step I data-taking, by measuring their emittance [7] and assessing their pion contamination [8].

Each TOF station is made of two planes of fast 1" thick scintillator counters along X/Y directions (to increase measurement redundancy) read out at both edges by R4998 Hamamatsu fast photomultiplier tubes<sup>1</sup>. R4998 PMTs have been delivered by Hamamatsu in assemblies (H6533MOD) that include the PMT tube, the voltage divider chain and a 1 mm thick  $\mu$ -metal shield, extending 30 mm beyond the photocathode surface. TheTo increase the count rate stability active dividers were used, instead of conventional resistive ones. A simple design with flat fish-tail PMMA light guides, as respectopposed to tilted ones (to reduce the influence of magnetic field) or Winston cones, has been chosen to optimize the timing detector resolution (favouring the collection of straight light) and to allow an easy mechanical assembly. any picture or reference here? TOF0, TOF1, and TOF2 have active areas of  $40 \times 40 \text{ cm}^2$ ,  $42 \times 42 \text{ cm}^2$ , and  $60 \times 60 \text{ cm}^2$  respectively. The slabs in TOF0 are 4 cm wide, while the slabs of TOF1 and TOF2 are 6 cm wide respectively. The PMTs signal, after ~34 m long RG213 cable and a 50% – 50% passive splitter, arrive to a leading-edge CAMAC Lecroy 4115 100 discriminator followed by a CAEN V1290 TDC for time measurements and to a CAEN V1724 FADC for

<sup>1</sup>one-inch linear focused PMTs with 10 stages, typical gain  $G \sim 5.7 \times 10^6$  at -2250 V and B=0 T, rise time 0.7 ns, transit time spread (TTS)  $\sim 160 \text{ ps}$

pulse-height measurements, to correct time-walk. As reported in reference [2], RG213 cables<sup>2</sup> have a better temperature stability than conventional RG58 cables. Their delay have been individually measured in laboratory, before installation in the experimental hall. Time calibration of individual counters has been done with impinging beam particles by using the detector X/Y redundancy [9]. *This is too vague. Calibration will be covered later. What does counter refer to here?*

Due to the low residual magnetic field produced by the last quadrupole of the beam line in the proximity of the TOF0 detector ( $\leq 50$  G), the used conventional PMTs had to use elongated  $\mu$ -metal shielding. The other two TOF stations (TOF1/TOF2) had to work instead in the stray fields of the cooling channel solenoids, that are only partially shielded by a 100 mm thick annular iron plates. As residual magnetic fields are up to 0.13 T (with a component along the PMTs axis up to 0.04 T), a local or global magnetic shielding for TOF1 and TOF2 detectors had to be envisaged. The local shielding option was chosen, at the end, for convenience and easiness of implementation. As magnetic shielding is a mass effect, box-shaped soft iron shielding are more effective than cylindrical ones. This idea pioneered in the D0 experiment has been tested in the case of MICE using different geometrical configuration for the iron shielding boxes and different iron materials (e.g. Fe360, ARMCO<sup>3</sup>, etc). The problem is usually the longitudinal component of the magnetic field, while the orthogonal component may be more easily shielded. Systematic studies have been done, using a built on purpose solenoid of 23 cm inner diameter, 40 cm length<sup>4</sup> and are fully reported in reference [10]. A composite structure based on the 1 mm  $\mu$ -metal shielding of the H6533Mod assemblies and an external additional  $6 \times 6 \text{ cm}^2$  ( $5.6 \times 5.6 \text{ cm}^2$ ) ARMCO box, 15 cm long, with an internal hole of 3.2 cm diameter has been adopted for the PMT's magnetic shielding of TOF2 (TOF1) [11]. Fig. 1 show how the local shielding has been implemented in TOF2, using different sheets of ARMCO to make a “single bar structure” for all the PMTs of one side, instead of single boxes for individual PMTs. The effective shielding amounts to  $\sim 6.6$  cm of ARMCO thickness, with extra shielding effect due to the fact that all bars shielding the TOF2 PMTs are magnetically linked between them and to both the KL shielding and the shielding plate making a single magnetic loop. Fig. 2 shows some steps of the assembly procedure for the TOF2 detector at INFN MIB mechanics workshop.

*The paragraph above is rather detailed, with many things that could be explained incorrectly. Should be made brief, unless full technical design description is required.*

*The following paragraph is summarising the performance. It states overly optimistic performance.*

*reformulate — For what attains performances—, TOF0, TOF1, and TOF2 had timing resolutions around 50-60 ps respectively (*currently observed  $\sim 110$  ps*), over the 8 years running period, consistent with design requirements, with the spatial resolution around 1 cm. *We don't use any special reconstruction method. Resolution kept at 4 cm or 6 cm for TOF0 or TOF1 and TOF2 respectively. Do we say resolution = 1/2 of strip width or  $1/\sqrt{12}$ ?* Fig. 3 shows distributions of the time of flight between TOF0 and TOF1 where electrons, muons and pions fall into three well defined peaks.*

*What is currently the main purpose of TOFs? This determines the requirements on the performance. Will need to tell that current T-o-F measurement has sufficient resolution, which appears to be  $\sim 100\text{-}120$  ps*

Error of the time-of-flight measurement is a combination of intrinsic resolution of each TOF station and errors in the calibrations of individual *scintillation counters*. The total error of t-o-f as measured by stations  $i$  and  $j$  is considered as:

$$\sigma_{\text{TOF}_{ij}} = \sqrt{\sigma_i^2 + \sigma_j^2 + \sigma_{\text{calib}}^2}. \quad (1)$$

Individual uncertainties  $\sigma_i$  are assumed to be statistically uncorrelated. Error of the calibration method,  $\sigma_{\text{calib}}$ , consists of uncertainties correlated and uncorrelated between the stations.

---

<sup>2</sup>CERN type C-50-6-1, with rated delay 4.08 ns/m

<sup>3</sup>ARMCO steel from AkSteel is a pure iron with a maximal carbon content of 0.025% and very high magnetic saturation

<sup>4</sup>built by TBM srl, Ubondo (VA), Italy

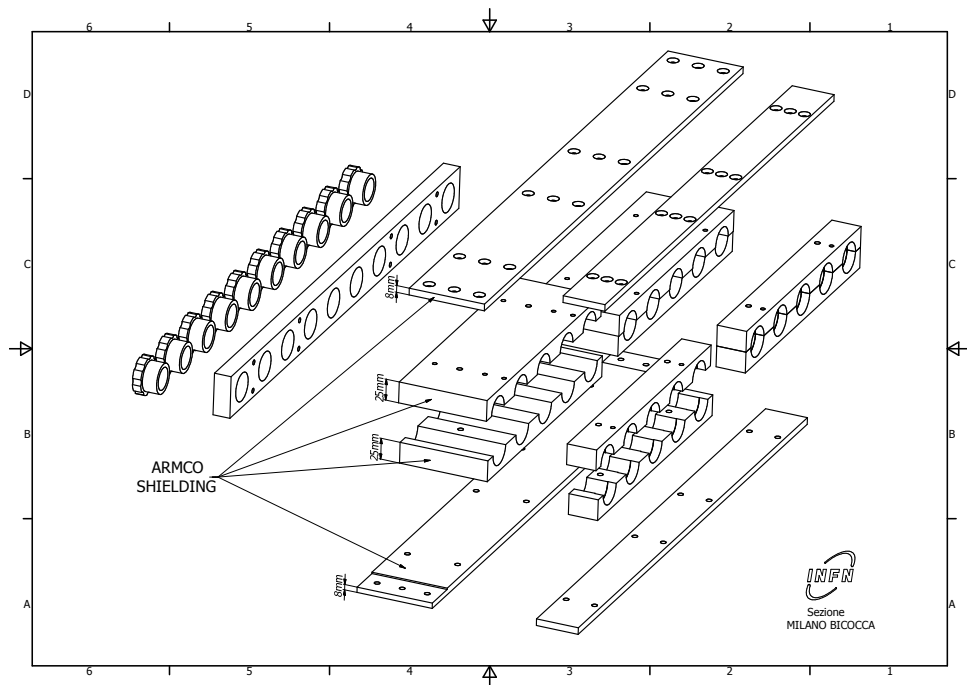


Figure 1: Exploded view of the TOF2 detector magnetic shielding for one row of PMTs.



Figure 2: Assembly of TOF2 at INFN MIB mechanics workshop. Left to right: from the bare magnetic shielding to the installed counters of a plane.

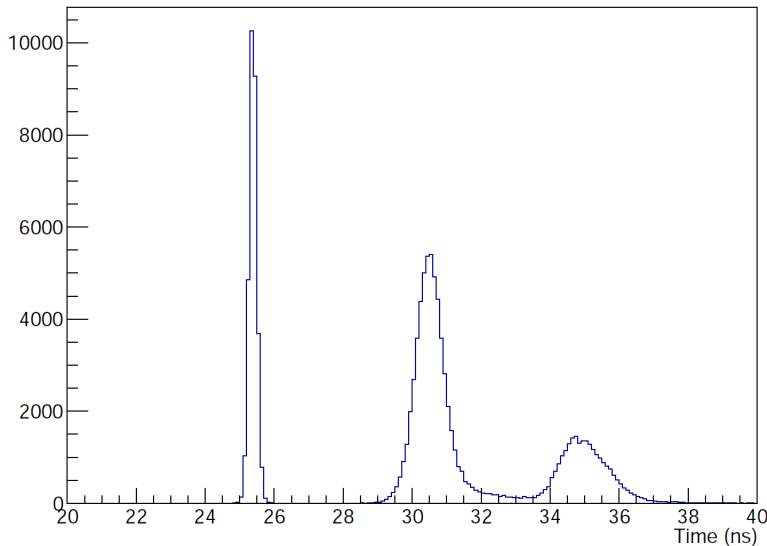


Figure 3: Time of flight between TOF0 and TOF1 for a “pion” beam. From the left: the well separated electron, muon and pion peaks.

## 2.2 TEMPORARY - Plots

### <sup>140</sup> 2.3 Calibration Method

- Describe the method. Based on MICE note 251.
- *TOF NIMA paper says that measured time resolution of the CAEN TDC was 22 ps/count, as opposed to declared 25 ps!*
- Some description of the calibration method is also described in the paper.
- *There's a short description of the method also in Rayner's Thesis, Section 3.2.1 and Appendix B (this is improved method to extract more calibration constants for proper x,y measurements, Rayner claims ~1 cm resolution; our current resolution = slab width / sqrt(12) ~ 1.2 – 1.7 ).*

<sup>150</sup> Measurement of time traversal of a particle through a TOF station is influenced by several factors at the hardware level. When a particle crosses the plastic scintillator, there is a short delay in light production. There are often at least two components to the light: the first one is fast with a characteristic scintillation time of  $\sim 1$  ns, and second being much slower with characteristic time  $\sim 10$  ns (*double check the times*). Contribution of each component changes with the ionisation density and hence with particle type.

<sup>155</sup> After generation, scintillation light propagates to the ends of each scintillator slab where it is detected by photomultiplier tubes. The light-travel time depends on the distance of the particle crossing from the PMT. The length of slabs in TOF0, TOF1, and TOF2 are 40 cm, 42 cm, and 60 cm, respectively. This translates to about 3 ns, 3.1 ns, and 4.4 ns, respectively, as the effective light propagation speed in the scintillator was found to be approximately 13.5 cm/ns.

<sup>160</sup> Next delays are introduced by the transit times of each PMT and the cable that lead the signal to the electronics. These times are specific for each individual PMT channel and needs to be determined in dedicated measurements.

The times of each signal of a PMT are measured as times of signal threshold crossings in a simple linear discriminator. This introduces bias in the measured time dependent on the total charge of the signal, effect referred to as time-walk.

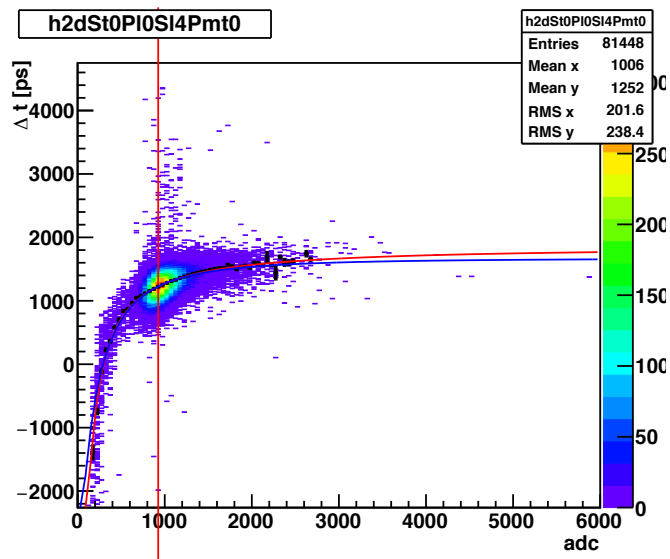


Figure 4:

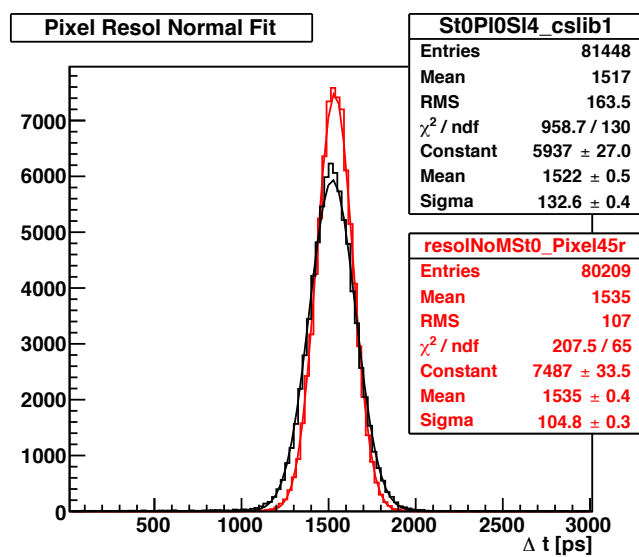


Figure 5:

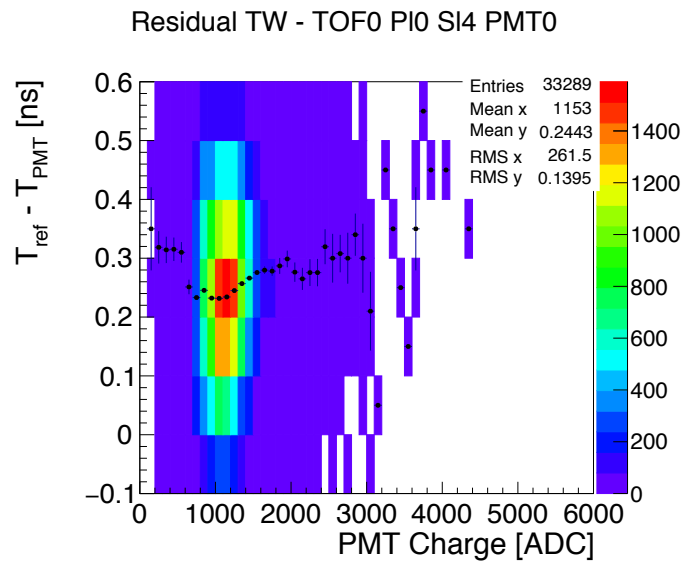


Figure 6:

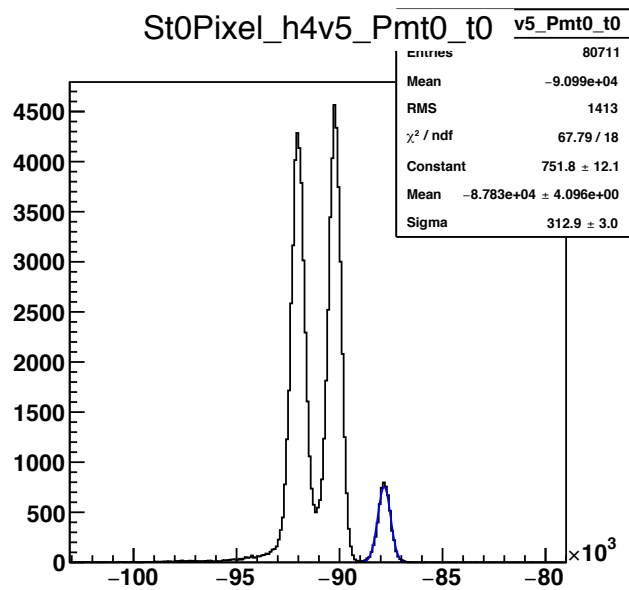


Figure 7:

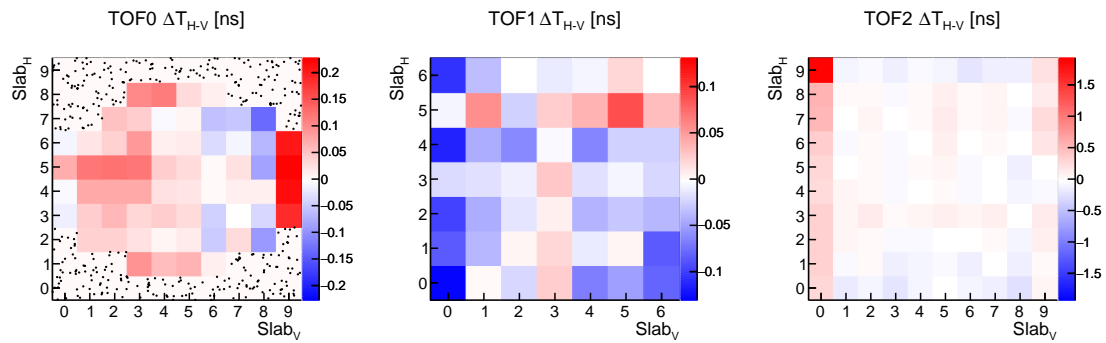


Figure 8:

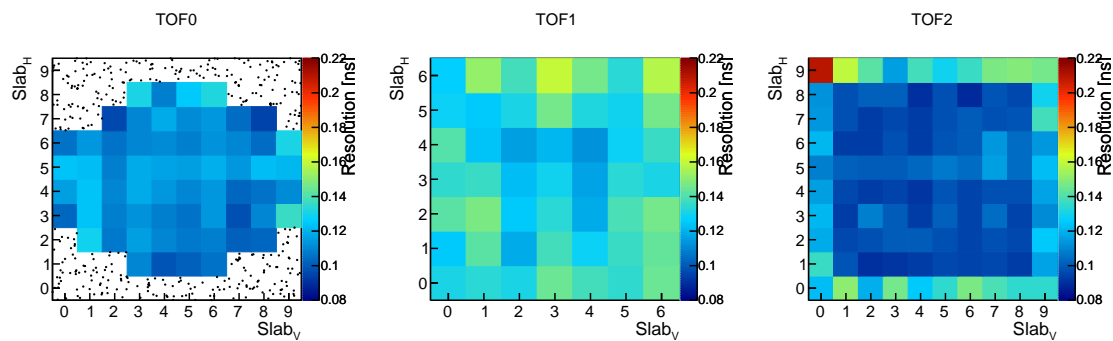


Figure 9:

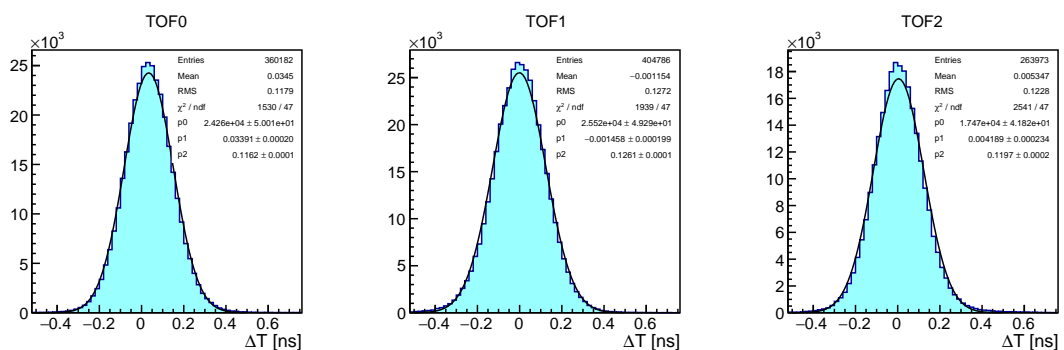


Figure 10:

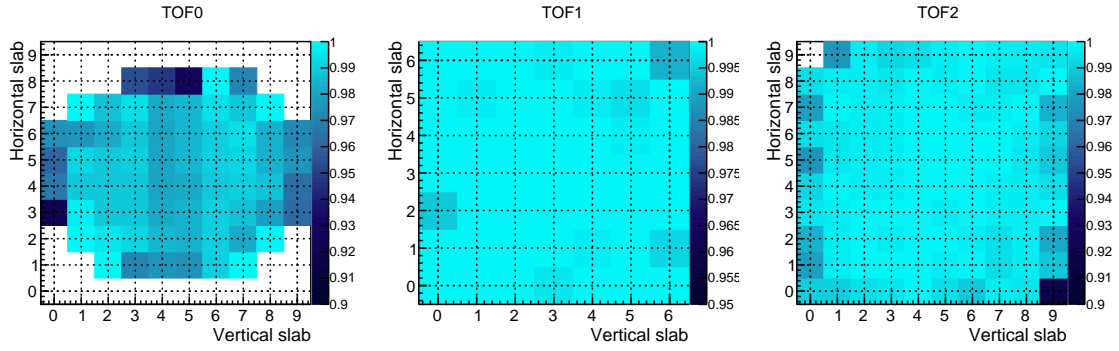


Figure 11:

Signal times of each channel are recorded in TDC boards. Readout of the whole system is triggered by having  
 165 a signal in TOF1 station. Time of the channel that caused the readout is also recorded in each TDC board and is used as a reference time. Depending on where the particle crosses through TOF1 station, this trigger time will be issued by different PMTs, and consequently the reference time will have a bias dependent on the position of TOF1 crossing.

The final time measurement in each station determined as an average of the times of individual channels.  
 170 This way, different distance from the point of crossing to each side of the scintillator slabs does not matter anymore, because the average of the times of the 2 PMTs does not depend on it.

Corrections which need to be made to the measured times are then the time-walk correction, PMT channel specific delay time  $T_0$ , and correction for reference trigger time delay.

### 2.3.1 Time-walk Correction

- 175 • *Fig of a selected PMT TW 2D hist. + Profile + Fit*  
 • *Fig of residual TW.*  
 • *Fig of Slab DT before TW correction and after.*

Time walk was considered to be constant property of each channel. The same correction was used for all runs.

First correction to the measured time of each channel is time-walk correction. The correction was determined  
 180 by looking time difference between two selected channels from two crossing slabs.

Correction was first determined for reference slabs, middle slabs in each plane. Pixel corresponding to their crossing was always well populated with particles crossing it which provided large statistics to limit the charge in one of the slabs to a small region around its maximum and to use it as reference time which was little affected by the time walk. Time walk of PMTs in the other slab could easily be determined from the measured time  
 185 with respect to the limited reference channel.

After provisional determination of time-walk of the reference slabs, time-walk of all the PMT channels was determined by looking at events in pixels corresponding to the crossing with the reference slab.

A time-walk correction curve was fitted to the data. First, a profile was created and then function

$$f(\text{ADC}) = P_1 + \frac{P_2}{\text{ADC} - P_0} + \frac{P_3}{(\text{ADC} - P_0)^2}. \quad (2)$$

Where possible, parameter  $P_3$  was fixed to 0. For some PMTs such fit would not follow the measured trend and the additional parameter was added to the fit.

190 Example of time-walk in a reference channel after the first round of reference calibrations is in Figure X.  
Example of time walk of a channel with respect to pre-corrected time in a reference slab is shown in Figure Y.

Figure Z shows distributions of time differences between horizontal slab 4 and vertical slab 5 before and after time walk correction. The width of the distribution is significantly decreased. The mean of the distribution is not centered at 0 as differences in delays  $T_0$  due to individual PMTs and their cables were not accounted for,  
195 yet.

### 2.3.2 Trigger Delay Correction

Station TOF1 was used to trigger readout of the whole system. Time of its trigger signal was used as a reference signal to which times of each channel of all 3 stations were measured. Two-fold coincidence of signals crossing threshold in PMTs on both sides of a slab is required. For an incoming particle the trigger signal is given by  
200 the first of the twofold coincidences from slab i and slab k. The time of the coincidence signal is the time of the latest signal arriving to the logic unit. Which PMT channel will be causing trigger depends on the position within the slab of the particle crossing and the  $T_0$  delays of individual PMTs. Assuming that light arrival time does not change significantly across a pixel and no other effects influence signal arrival one can expect that  
205 passage of a particle through a given pixel causes always the same time sequence of PMT signals and the delay of the trigger signal will be that of one particular channel in each pixel. This assumption, however, does not hold for all pixels. The main reason being the time walk effect which biases each channel differently and in some pixels results in more than 1 PMT channel generating the trigger signal.

The trigger signal delay of each pixel was measured relative to the central pixel of TOF1 station. Times of each PMT were corrected for time walk first. Mean times of PMTs in reference slabs, horizontal slab 3 and  
210 vertical slab 3, were compared for each pixel.

$$t_{\text{TW}i,j}^{\text{PMT}}$$

$$\frac{1}{2} \sum_{\text{PMT}} \langle t_{\text{TW}3,j}^{\text{PMT}} \rangle - \langle t_{\text{TW}3,3}^{\text{PMT}} \rangle \quad (3)$$

$$\frac{1}{2} \sum_{\text{PMT}} \langle t_{\text{TW}i,3}^{\text{PMT}} \rangle - \langle t_{\text{TW}3,3}^{\text{PMT}} \rangle \quad (4)$$

$$\frac{1}{4} \sum_{\text{PMT}} (\langle t_{\text{TW}i,j}^{\text{PMT}} \rangle - \langle t_{\text{TW}i,3}^{\text{PMT}} \rangle + \langle t_{\text{TW}i,j}^{\text{PMT}} \rangle - \langle t_{\text{TW}3,3}^{\text{PMT}} \rangle) \quad (5)$$

For pixels not defined by the reference slabs, we can compare estimated delay times  $T_{\text{tr}}^{i \neq 3, j \neq 3}$  arrived to from the vertical and horizontal reference slab, 1st and 2nd part of Equation (5), respectively.

215 Figure X shows comparison of time-walk corrected recorded times in a channel for particles passing through different pixels. The variation in position of the peaked distributions is clearly visible.

Figure Y shows times measured in a channel in TOF0 station for particles crossing the station's central pixel (4,5). Times before correction for the trigger signal delay are compared to times after the correction.

### 2.3.3 $T_0$ Correction

220 Times in each channel were corrected for the channel specific delays caused by each PMT and by cable lengths. The correction was extracted from channel times corrected for time walk and trigger signal delay. After that, TOF1 stations' times differ only by the channel specific delays. Constant offsets were applied such that time distributions in TOF1 were centered at 0.

Times in TOF0 and TOF2 stations reflected the time of flight of individual particles to and from TOF1 and the channel delays  $T_0$ . Distribution of the times in those station show 3-peaked structure, where the most isolated peak at lowest tome-of-flight corresponds to electrons in the beam which travel at speed of light. Their time of flight was calculated from distances from TOF1 station, 8.XX m and 8.xx m for TOF0 and TOF1, respectively. Figure Y shows position of the electron peak in one channel of TOF0 before and after the last correction. Right hand side of the figure compares time distribution of all channels before and after the correction.

Due to the presence of focusing fields in the beam-line section between TOF0 and TOF1 stations, particles did not travel in a straight line in that section. Deviation from a straight line was dependent on the initial direction and momentum of the particles entering the section. The effect was estimated [?] in simulations to be of an order of  $\sim 30$  ps. This effect caused a small bias in the calibrations.

## 2.4 Reconstruction

- slab hits - must have PMT over threshold on both sides
- only first recorded hits in the readout (per trigger) are considered
- times corrected for TW, TrigT and  $T_0$
- corrected slab time is the average of corrected times of each PMT
- “Space Point” (SP) is created for each combination of 2 cross slabs where the corrected slab times fall within 3 ns.
- coordinate of the SP is placed in the middle of the station along the beam axis (where the two slab planes touch each other) and in the center of the slabs in the transverse direction.
- the time of the SP is the average of the slab times of the slabs it was reconstructed from.

Recorded signals in all PMT channels are processed in the following way. First, signals in opposite PMTs of a slab are paired. Recorded times are corrected for time walk, channel delay  $T_0$ , and for the delay of the trigger signal. This requires that the trigger pixel in TOF1 station is determined.

Pixel area where the particle crossed the station is searched by attempting to match all possible combinations of slab signals in each plane. Transverse slabs are matched if their corrected times fall within a 4-ns window. A space point is then created with spatial coordinates centered at centre of the pixel in the transversal direction and middle of the station in the longitudinal direction. Time of the space point is calculated as an average of the times of each slab.

## 2.5 Performance

*Several figures are already in the TOF NIMA paper.*

Figures to show here:

- Slab DT - selected slabs/counters + overall TOFs
- ToF10 - + detail of electron peak
  - will need to argue why the peak is broader than stated resolution
  - the effect of electron's flight path due to focusing fields is non-negligible - use estimates from Rayner's thesis
- Space-point reconstruction efficiency
  - shows that slab hits are within the required cut
    - \* events with 2 slab hits only
  - inefficiency from:
    - \* only single slab hit by different particles in the given spill/bunch

- 265                    \* this may be due to inefficiency of hit creation when particle crosses by the edge of the slab – see  
                       Rayner’s thesis/presentations
- 270                    \* two particles share one slab - earlier particle’s hit only considered - but this is not considered in  
                       these plots (only 2 slab hits recorded)
- Stability of electron peak - run by run position of electron peak!
  - particle detection efficiency - how to show?
  - Resolution
    - Slab DT for all TOFs, show similar performance, although they have different construction.
  - (**?**)Efficiency

### 2.5.1 Low-level Characterisation

275 *maybe leave this out, likely not necessary*

- PMT charge correlation PMT0 vs PMT1 - maybe, if relevant
- Residual TW - this should go to the calibration section
- Slab DT

## 3 Cherenkov Detectors

### 280 3.1 Introduction

The Cherenkov detectors are primarily designed to provide  $\pi$ - $\mu$  separation in the higher momentum ranges, where TOF separation is not sufficient for conclusive particle identification.

In order to provide separation over a large range of momenta, two high density silica aerogel Cherenkov detectors (CkovA and CkovB) with refractive indices  $n=1.07$  and  $n=1.12$  are used. They are each read out by 285 four 200 mm photomultiplier tubes and placed directly one after another in the beamline, located just after the first TOF counter. In Fig. 12 an exploded view of one detector is shown.

Their respective thresholds provide different responses in four distinct momentum ranges, i.e. in the 200 MeV/c beams, pions are below the threshold which would fire the detector for both CkovA and CkovB whereas muons are above only for CkovB, while for the 240 MeV/c beams, pions are above the threshold for CkovB 290 while muons are above for both CkovA and CkovB. Using this information algorithms can be written that produce likelihood distributions of particle type. Below the CkovB muon threshold of about 217.9 MeV/c, where there is no separation, the TOFs provide good separation, whereas the momentum range above the CkovA pion threshold (367.9) MeV/c is outside of the MICE running parameters [12].

### 3.2 Performance

## 295 4 KLOE-Light Calorimeter

### 4.1 Introduction

The KLOE-Light (KL) pre-shower sampling calorimeter is composed of extruded lead foils in which scintillating fibres are placed in volume ratio scintillator:lead  $\sim 2:1$ , “lighter” than the one of the KLOE experiment calorimeter (1:1).

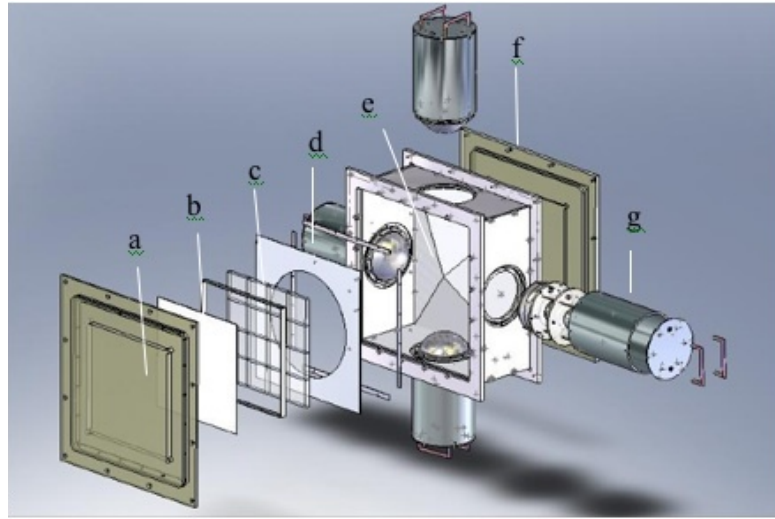


Figure 12: MICE aerogel Cherenkov counter blowup: a) entrance window, b) mirror, c) aerogel mosaic, d) acetate window, e) GORE reflector panel, f) exit window and g) 8 inch PMT in iron shield.

300 The fibres are 1 mm diameter BICRON BCF-12, scintillating in the blue, 1.35 mm distant from each other  
 within a layer. The distance between two layers is 0.98 mm, one layer being shifted by half the fibre pitch with  
 respect to the next. Scintillation light is guided from each slab into a total of six PMTs (three on each side).  
 Iron shields are fitted to each photomultiplier to mitigate against large stray magnetic fields from the cooling  
 channel (see Fig. 13). The signal from each PMT is sent to a shaping amplifier (SA) module, which shapes and  
 305 stretches the signal in time in order to match the sampling rate of the flash ADCs (Fig. 14 shows the design of  
 a single slab). A total of 7 slabs forms the whole detector, which has an active volume of 93 cm×93 cm×4 cm.

With its 2.5 radiation lengths the KL is used to distinguish muons from decay electrons providing energy deposition and timing information and to act as pre-shower in front of the EMR. The detector has been used to estimate the level of pion contamination within the MICE muon beams to be around 1% [8].

## 310 4.2 Performance

The study of KL response to different particle types at different momenta is based on particle identification obtained by time-of-flight detector, as shown in the example of Fig. 3, by applying proper cuts on the time-of-flight spectrum. The performance is presented for 140, 170, 200, 240 and 300 MeV/c momenta at the absorber position, and depending of species population for muons, pions and electrons. The results presented below are 315 obtained from the straight tracks data (i.e. without magnetic fields in the trackers or focus coil) taken mainly in 2017. The KL response to muons, pions and electrons for all available momenta is presented in Fig. 15. It is clear in the cases of muons and pions that they are below mip momenta since energy deposition decreases with momentum increasing<sup>5</sup>.

For comparison of energy deposition of muon, pions and electrons for fixed momentum Fig. 16 is presented.  
 320 In the case of 300 MeV/c (Fig. 16, right), where muons and pions have almost the same maximum of distribution, the tail of pions is fatter than muon one. This is due to the fact that pions experience strong interaction as

<sup>5</sup>Actually the energy deposition is defined as the sum of ADC products from all cells in KL above a given threshold. The ADC product on the other hand is the product of left and right side of one slab divided by the sum of left and right side:  $ADC_{prod} = 2 \times ADC_{left} \times ADC_{right} / (ADC_{left} + ADC_{right})$ . The factor 2 is present for normalization. The product of two sides compensates the effect of attenuation.

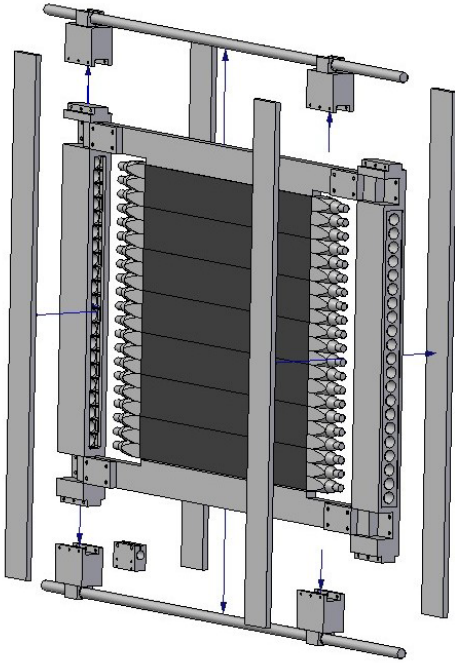


Figure 13: Magnetic shielding of KLOE-Light PMTs.

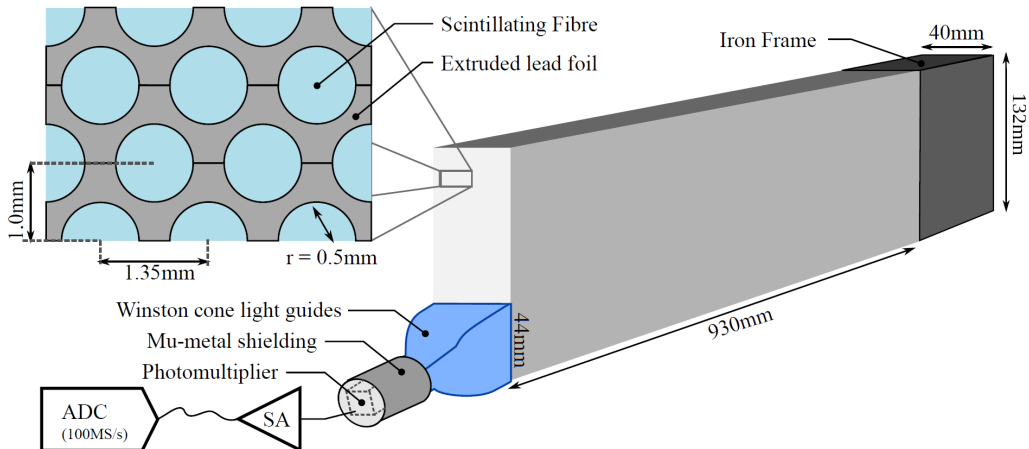


Figure 14: Single slab design of MICE KLOE-Light Calorimeter.

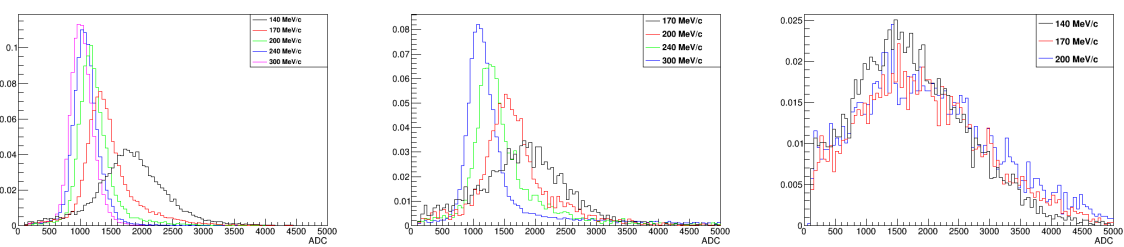


Figure 15: KL response to muons (left), pions (centre) and electrons (right) for several momenta. It is shown charge deposited by particles in KL in arbitrary units. All histograms are normalized to unity.

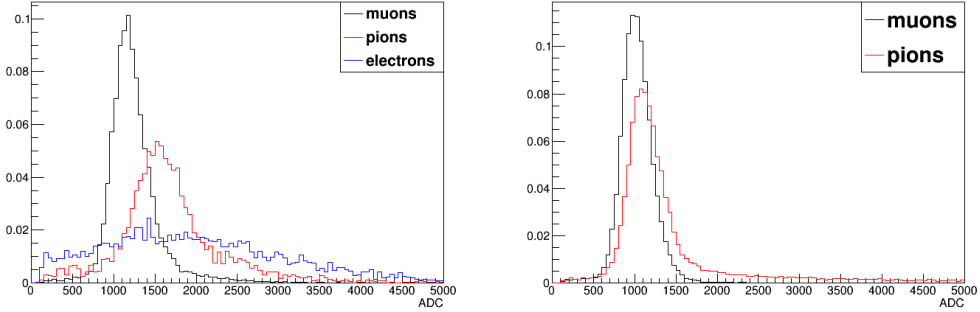


Figure 16: Comparison of energy deposition of muons, pions and electrons at 200 MeV/c (left) and of muons to pions at 300 MeV/c (right).

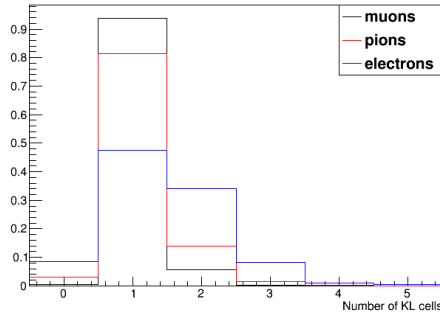


Figure 17: Particle multiplicity for 240 MeV/c, i.e. number of KL cells fired.

well. This pion behaviour has been used to estimate its contamination in muon sample.

The number of fired KL cells by a single muon, electron or pion is given in Fig. 17 for 240 MeV/c beam. For muons we expect one, in some cases two and almost never more fired cells depending on track inclination. For pions and electrons create avalanches in KL and electron ones is much wider than the pion ones as visible of number of KL cell hits. The same figure shows number of events when if there is a reconstructed TOF track, but no signal in KL above the threshold. This can be used to calculate efficiency of KL for the three species as a function of momentum. The results are presented in Table 2 and shows that efficiency for muon registration is close to 99%.

<b>species</b>	<b>140 MeV/c</b>	<b>170 MeV/c</b>	<b>200 MeV/c</b>	<b>240 MeV/c</b>	<b>300 MeV/c</b>
<b>electrons</b>	$0.95 \pm 0.02$	$0.95 \pm 0.01$	$0.94 \pm 0.03$	n/a	n/a
<b>muons</b>	$0.97 \pm 0.02$	$0.99 \pm 0.01$	$0.99 \pm 0.01$	$0.99 \pm 0.01$	$0.99 \pm 0.01$
<b>pions</b>	n/a	$0.89 \pm 0.03$	$0.95 \pm 0.03$	$0.97 \pm 0.03$	$0.98 \pm 0.01$

Table 2: Efficiency of KL for electrons, muons and pions as a function of particle momentum. The conditions required are existing of a TOF track and signal in KL above the threshold. The uncertainties are statistical.

In Fig. 18 is shown simulation of KL response to 300 MeV/c muons and pions and the distributions are compared with data. The agreement between data and simulation is very good. The simulation is done via following steps:

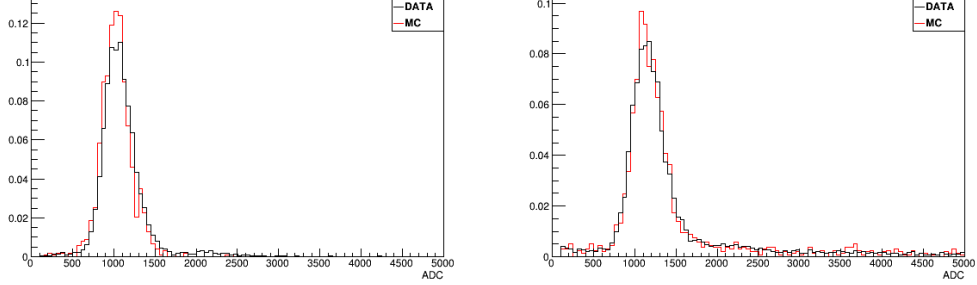


Figure 18: Comparison between data and Monte Carlo simulation of KL response to muons (left) and pions (right) at 300 MeV/c.

- Smearing of produced photons in scintillator fibres. They obtain Poisson statistic so such is applied. In principle one can replace it with Gaussian because the number of photons created is large enough for such an approximation.
- Photoelectrons created on photomultiplier photocathode also have Poisson statistics. It cannot be replaced here with normal distribution because the number of photoelectrons is small enough so such an approximation is illegal.
- Photomultiplier gain obtains also statistical properties but it is neither Poisson nor gauss. Nevertheless it turns out that for simplicity one can use Gaussian distribution with mean value equals to PMT gain and sigma of distribution equals to half of the gain. KL photomultipliers have gain  $\sim 2 \times 10^6$ , so their sigma is simply  $10^6$ .

## 5 Electron Muon Ranger

### 5.1 Introduction

The Electron-Muon Ranger (EMR) is a fully-active scintillator detector [13]. It can be classified as a tracking-calorimeter as its granularity allows for track reconstruction. The EMR consists of extruded triangular scintillator bars arranged in planes. One plane contains 59 bars and covers an area of  $1.27 \text{ m}^2$ . Each even bar is rotated by 180 degrees with respect to the odd one. A cross-section of bars and their arrangement in a plane is shown in Fig. 19. This configuration does not leave dead area in the detector for particles crossing a plane with angles that do not exceed 45 degrees with respect to the beam axis. Each plane is rotated through 90 degrees with respect to the previous one, such that a pair of planes defines a horizontal and vertical ( $x, y$ ) interaction coordinate. The light, produced when a particle crosses a bar, is collected by a wave-length shifting (WLS) fibre glued inside the bar. At both ends, the WLS fibre is coupled to clear fibres that transport the light to a photomultiplier tube (PMT). Signals produced in a plane are read out collectively on one end by a single-anode PMT for an integrated charge measurement and separately on the other by a multi-anode PMTs for individual bar hit reconstruction. The full detector is composed of 24 X-Y modules for a total active volume of  $\sim 1 \text{ m}^3$ .

An array of analyses were conducted to characterize the hardware of the EMR and determine whether the detector performs to specifications [14]. The clear fibres coming from the bars were shown to transmit the desired amount of light, and only four dead channels were identified in the electronics. Two channels had indubitably been mismatched during assembly and the DAQ channel map was subsequently corrected. The level of crosstalk is within acceptable values for the type of multi-anode photomultiplier used with an average of  $0.20 \pm 0.03\%$  probability of occurrence in adjacent channels and a mean amplitude equivalent to  $4.5 \pm 0.1\%$

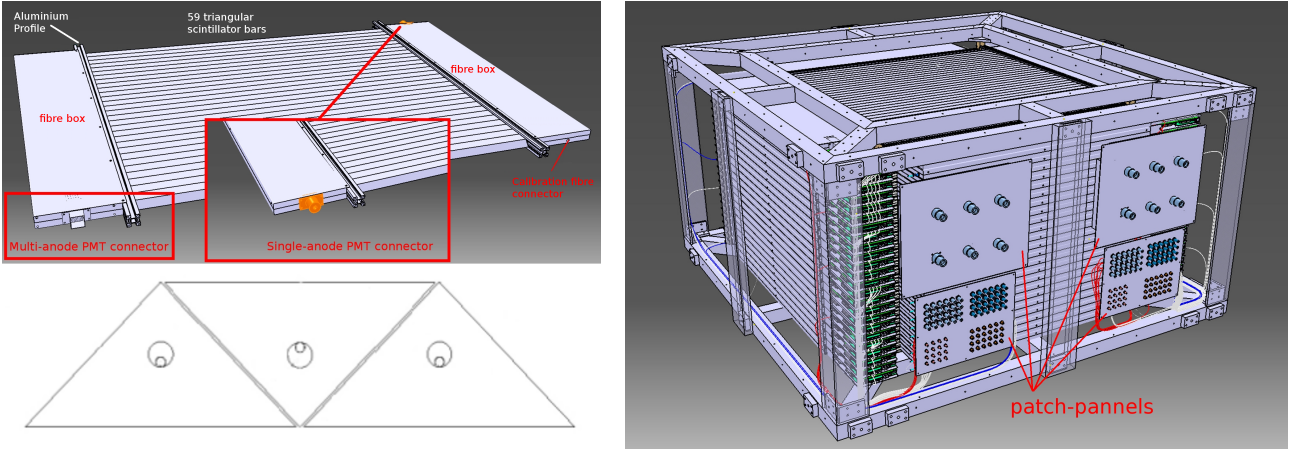


Figure 19: Drawing of one EMR plane (top left), cross section of 3 bars and their wavelength shifting fibres (bottom left) and drawing of the full detector and its supporting structure (right).

of the primary signal intensity. The efficiency of the signal acquisition, defined as the probability of recording a signal in a plane when a particle goes through it in beam conditions, reached  $99.73 \pm 0.02\%$ .

365 The primary purpose of the EMR is to distinguish between muons and their decay products, identifying muons that have crossed the entire cooling channel. Muons and electrons exhibit distinct behaviours in the detector. A muon follows a single straight track before either stopping or exiting the scintillating volume, while electrons shower in the lead of the KL and create a broad cascade of secondary particles. Two main geometric variables, the plane density and the shower spread, are used to differentiate them. The detector  
 370 is capable of identifying electrons with an efficiency of 98.6 %, providing a purity for the MICE beam that exceeds 99.8 %. The EMR also proved to be a powerful tool for the reconstruction of muon momenta in the range 100–280 MeV/c [15].

## 5.2 Performance

375 The performance of the EMR detector is assessed at three levels of resolution with the data acquired during the 2017/02 and 2017/03 ISIS user cycles. The performance of the hardware itself is evaluated by analysing the characteristics of raw photomultiplier signals. The reconstruction efficiency is assessed by looking at higher level quantities. The performance of the detector as an electron tagging device is measured.

### 5.2.1 Hardware efficiencies

380 The data sets used to evaluate the detector hardware efficiencies are summarized in table 3. The MICE beam line is tuned to the highest attainable momentum to maximize the transmission to the EMR detector and increase the range of particles in the detector. In this configuration, the beam line produces pions and muons in comparable quantities, along with positrons. The particle species are identified by evaluating their time-of-flight between TOF1 and TOF2. The time-of-flight distribution for muons, pions and positrons is represented in figure 20. Only the particles with a time-of-flight between 28 and 28.75 ns, i.e. compatible with the muon hypothesis, are  
 385 included in the analysis sample.

A muon that makes it into the analysis sample has a momentum larger than 350 MeV/c right before TOF2. It is expected to cross both TOF2 and the KL without stopping and penetrate the EMR. In practice, the probability

Run ID	Date	Type	Momentum	Spills	Triggers	EMR events
9619	19/09/2017	$\pi^+$	400 MeV/c	2289	265312	36775
9620	19/09/2017	$\pi^+$	400 MeV/c	5388	668026	107578
		<b>Total</b>		7677	933338	144353

Table 3: Summary of the data sets used to measure the efficiency of the EMR in the 2017/02 ISIS user cycle.

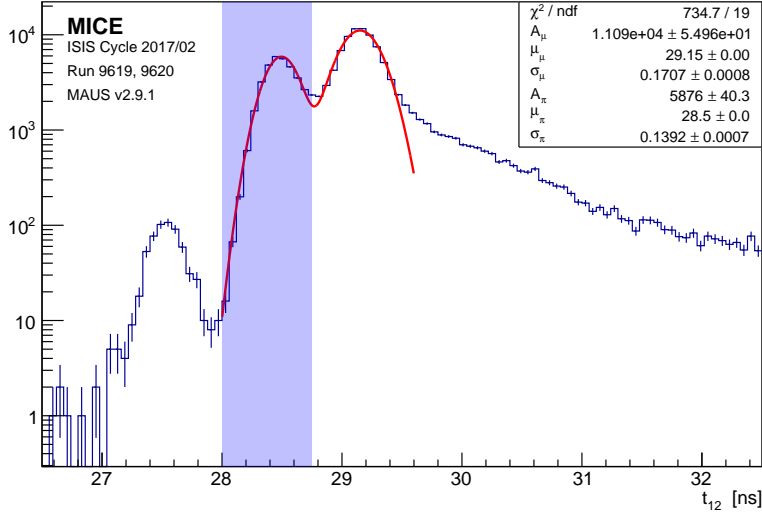


Figure 20: Time-of-flight of positrons, muons and pions for the 400 MeV/c pionic beam line used in the EMR efficiency analysis. The blue band represents the selected range.

of creating an EMR event, i.e. to produce hits in the detector is  $99.62 \pm 0.03\%$ . The minor inefficiency may be attributed to pions in the muon sample that experience hadronic interactions in the KL. If hits are produced in the detector, space points are reconstructed  $98.56 \pm 0.06\%$ . This inefficiency may be associated with muon that decay between TOF2 and the EMR and produce scarce hits in the detector.

To evaluate the efficiency of the scintillator planes and their readouts, only the muons which penetrate the entire detector are taken into account. If a signal is recorded in the most downstream plane, it is expected that at least a bar will be hit in each plane on its path and that a signal will be recorded in the single anode PMT. The left panel of figure 21 shows the MAPMT bar hit multiplicity for all the plane combined. It shows that in  $3.26 \pm 0.02\%$  of cases, on average, a plane traversed by a muon will be not produce a signal in its MAPMT and that the most probable amount of bars hit is one. The right panel shows the distribution of charge recorded in the all the SAPMTs. A track is missed by an SAPMT  $1.88 \pm 0.01\%$  of the time. This figure does not include SAPMT 26, turned off at the time of data taking.

Figure 22 shows the probability of recording a signal in individual MAPMTs and the SAPMTs for each of the 48 planes, given a muon that crosses the whole detector. The most inefficient PMTs miss the track  $\sim 10\%$  of the time. SAPMT 26 was experiencing issues during data taking and was turned off.

### 5.2.2 Electron rejection

The main purpose of the Electron-Muon Ranger is to tag and reject the muons that have decayed in flight inside the experimental apparatus. A broad range of beam line momentum settings, summarized in table 4, is used

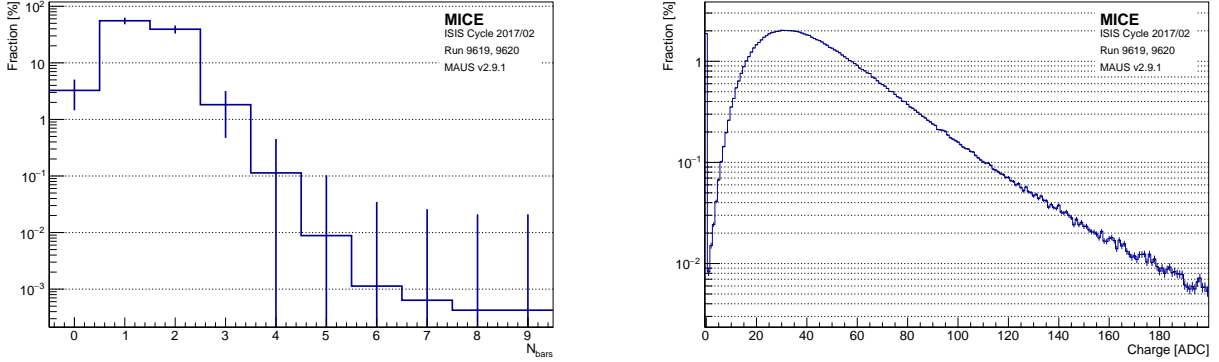


Figure 21: (Left) Global MAPMT bar multiplicity. (Right) Global SAPMT charge distribution.

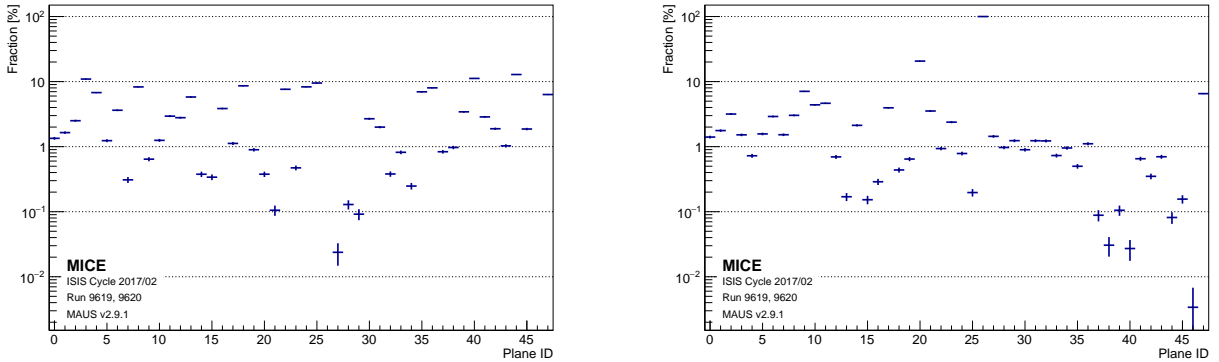


Figure 22: Probability of not producing a single bar hit in the MAPMT (left) and a zero charge in the SAPMT (right) in the 48 individual EMR planes.

to characterize its muon selection efficiency. The particle species is characterized upstream of the detector by using the time-of-flight between TOF1 and TOF2. It exhibits three distinct peaks consisting of positrons, muons and pions, respectively, in order of increasing time-of-flight. The distributions of time-of-flight are shown for the data sets in range 140–240 MeV/ $c$  in figure 23. The limits of the peaks are fitted to each setting in order to separate the muons and positrons into two templates upstream of the EMR. Particles that fall above the upper limit of the muon peak are either pions or slow muons and are rejected from this analysis.

MICE is a single-particle experiment, i.e. the signals associated with a trigger originate from a single particle traversing the detector. The multi-anode readout of each detector plane provides an estimate of the position of the particle track in the  $xz$  or the  $yz$  projection, depending on the orientation of the scintillator bars. Figure 24 shows event displays of a muon and a positron, as observed inside the detector, in the  $xz$  and  $yz$  projections for particles in the 240 MeV/ $c$  beam line setting. The muon exhibits a clean straight track while the positron showers inside the lead of the KL and produces a disjointed and widespread signature. The particle identification variables used in the EMR are based on these distinct characteristics.

The first particle identification statistic is the plane density,  $\rho_p$ , defined as

$$\rho_p = \frac{N_p}{Z_p + 1}, \quad (6)$$

with  $N_p$  the number of planes hit and  $Z_p$  the number of the most downstream plane. A muon deposits energy in

Run ID	Date	Type	Momentum	Spills	Triggers	EMR events
10268	26/11/2017	$\pi^+$	170 MeV/c	4418	328948	97452
10269	26/11/2017	$\pi^+$	170 MeV/c	3695	278330	82098
10262	25/11/2017	$\pi^+$	200 MeV/c	846	28103	8769
10266	25/11/2017	$\pi^+$	200 MeV/c	4365	148990	45448
10267	26/11/2017	$\pi^+$	200 MeV/c	4296	194207	53469
10275	26/11/2017	$\pi^+$	200 MeV/c	3547	126597	39114
10261	25/11/2017	$\pi^+$	240 MeV/c	4388	228337	66335
10264	25/11/2017	$\pi^+$	240 MeV/c	755	32322	10041
10265	25/11/2017	$\pi^+$	240 MeV/c	3336	134953	43129
10270	26/11/2017	$\pi^+$	240 MeV/c	222	17584	4030
10271	26/11/2017	$\pi^+$	240 MeV/c	66	5063	287
10272	26/11/2017	$\pi^+$	240 MeV/c	177	13538	1967
10273	26/11/2017	$\pi^+$	240 MeV/c	4339	232488	67350
10274	26/11/2017	$\pi^+$	240 MeV/c	738	38734	11123
<b>Total</b>				35188	1808194	530612

Table 4: Summary of the data sets used to measure the efficiency of the EMR in the 2017/02 ISIS user cycle.

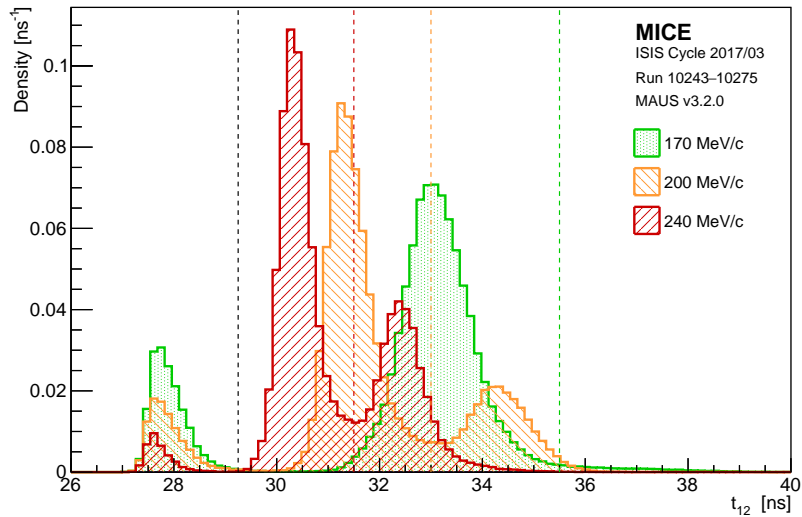


Figure 23: Time-of-flight distributions of the data sets in the range 170–240 MeV/c used in the EMR performance analysis. The dashed black line represents the upper bound of the positron peak and the coloured lines the upper bounds of the muon peaks in each setting.

every plane it crosses until it stops, producing a plane density close or equal to one. A positron shower contains photons that may produce hits deep inside the fiducial volume without leaving a trace on their path, reducing the plane density. The left panel of figure 25 shows the distribution of plane density of the muon and positron templates. The two templates occupy significantly different regions of plane density, as expected.

The second variable is the normalised chi squared,  $\hat{\chi}^2$ , of the fitted straight track, i.e.

$$\hat{\chi}^2 = \frac{1}{N-4} \sum_{i=1}^N \frac{\text{res}_{x,i}^2 + \text{res}_{y,i}^2}{\sigma_x^2 + \sigma_y^2}, \quad (7)$$

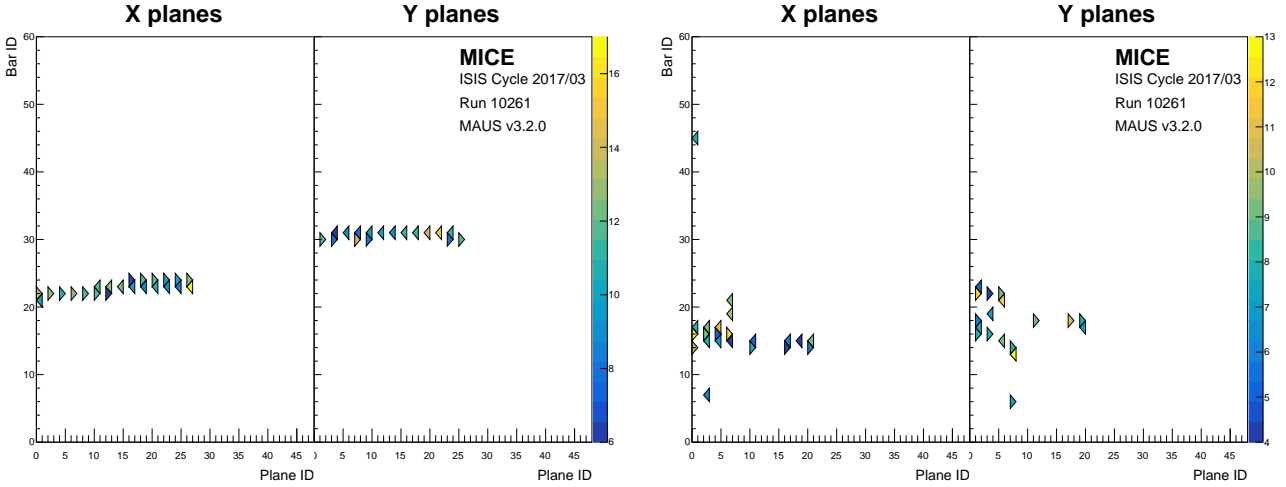


Figure 24: Event display of a muon (left) and a positron (right) from the 240 MeV/c beam line setting, in the  $xz$  and  $yz$  projections. The colour scale represents the time-over-threshold recorded in each channel, a digitized measurement of the energy deposition in the corresponding scintillator bar.

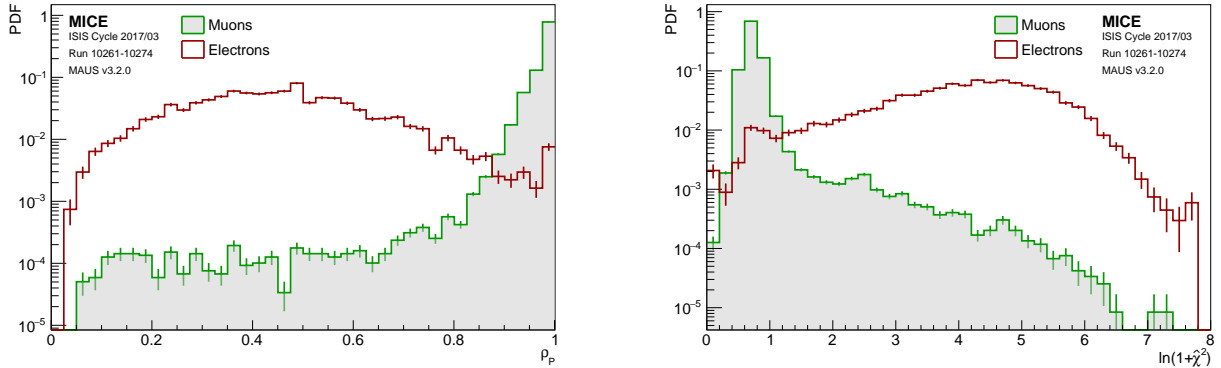


Figure 25: Plane density distribution,  $\rho_p$  (left), and normalised chi squared distribution,  $\hat{\chi}^2$  (right), of the muon and electron templates in the Electron-Muon Ranger.

with  $N$  the number of space points (one per bar hit),  $\text{res}_{q,i}$  the residual of the space point with respect to the  
425 track in the  $qz$  projection and  $\sigma_q$  the uncertainty on the space point in the  $qz$  projection,  $q = x, y$  [16]. The number of degrees of freedom is  $N - 4$ , as a three-dimensional straight track admits four parameters. This quantity represents the transversal spread of the particle's signature. A muon follows a single track and is expected to have a  $\hat{\chi}^2$  close to one, while an electron shower is expected to produce a larger value. The right panel of figure 25 shows the distribution of normalised chi squared of the muon and positron templates. The  
430 two templates occupy different regions of  $\hat{\chi}^2$  but overlap more than in the case of the plane density.

The two discriminating variables are combined to form a statistical test on the particle hypothesis. Given an unknown particle species, consider a set of cuts,  $(\rho_c, \hat{\chi}_c^2)$ , such that

$$\begin{aligned} \rho_p &> \rho_c \cap \hat{\chi}^2 < \hat{\chi}_c^2 \rightarrow \mu^+; \\ \rho_p &< \rho_c \cup \hat{\chi}^2 > \hat{\chi}_c^2 \rightarrow e^+. \end{aligned} \quad (8)$$

Dense and narrow events will be tagged as muons while non-continuous and wide electron showers will not.

The quality of a test statistic may be characterized in terms of the loss,  $\alpha$ , the fraction the muon sample that is rejected, and the contamination,  $\beta$ , the fraction of the electron sample that is selected. A test is optimal when the cost function,  $\Delta = \sqrt{\alpha^2 + \beta^2}$ , is minimized. Figure 26 shows the result of a scan over the parameter space. The left panel represents the cost,  $\Delta$ , as a function of the two parameters that define the test statistic. Each marker in the right panel represents the value of  $\alpha$  and  $\beta$  for the test values. The optimum choice of cuts yields a muon loss of 1.027 % and an electron contamination of 0.934 %.

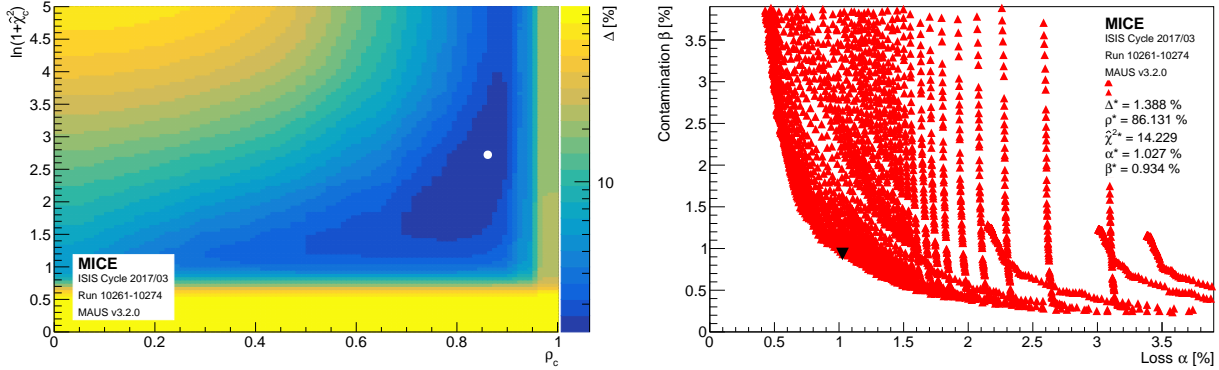


Figure 26: (Left) Cost function,  $\Delta = \sqrt{\alpha^2 + \beta^2}$ , as a function of the choice of cuts on the plane density and shower spread, ( $\rho_c, \hat{\chi}_c^2$ ). The white circle represents the minimum. (Right) Percentage of the electron sample tagged as muons ( $\beta$ ) as a function of the loss of real muons ( $\alpha$ ).

The downstream tracker (TKD) allows for the reconstruction of each particle momentum before entering the EMR. To assess the influence of momentum on contamination and loss, their values are calculated for 10 MeV/c bins in the range 100–300 MeV/c. The test statistic performed in each bin is based on the optimal set of cuts optimized for the whole sample, i.e.  $\rho^* = 86.131\%$  and  $\hat{\chi}^{2*} = 14.229$ . Figure 27 shows the loss,  $\alpha$ , and the contamination,  $\beta$ , as a function the TKD momentum. It shows that, at low momentum, the apparent muon loss increases. This is due to an increase in decay probability between TOF2 and the EMR and an decrease in the amount of muons that cross the KL to reach the EMR.

#### 5.2.3 Muon track momentum

The tracking capabilities of the detector enable the reconstruction of several muon parameters. Muons follow a straight track in the scintillating volume, continuously losing energy through ionization until they stop. The reconstructed track points are fitted with a straight line. The data summarized in table 4 is used to assess the tracking capability of the EMR. The left panel of figure 28 shows the distribution of origin track points, i.e. track positions at the entrance of the detector. The right panel shows the angular distribution of tracks, with respect to the  $z$  axis, as a function of the momentum reconstructed in the downstream tracker.

The end point of a muon track is reconstructed as the final space point in the most downstream plane reached by the particle. The length of the straight track that joins the origin of the track and its end point estimates the muon range. Figure 29 shows the range of muons in the EMR for different data sets and as a function of the momentum reconstructed from the muon time-of-flight between TOF1 and TOF2, i.e.

$$p_{12} = \frac{m_\mu c}{\sqrt{(ct_{12}/d)^2 - 1}}, \quad (9)$$

with  $m_\mu$  the muon mass,  $t_{12}$  the time-of-flight and  $d$  the distance between the two TOF stations.

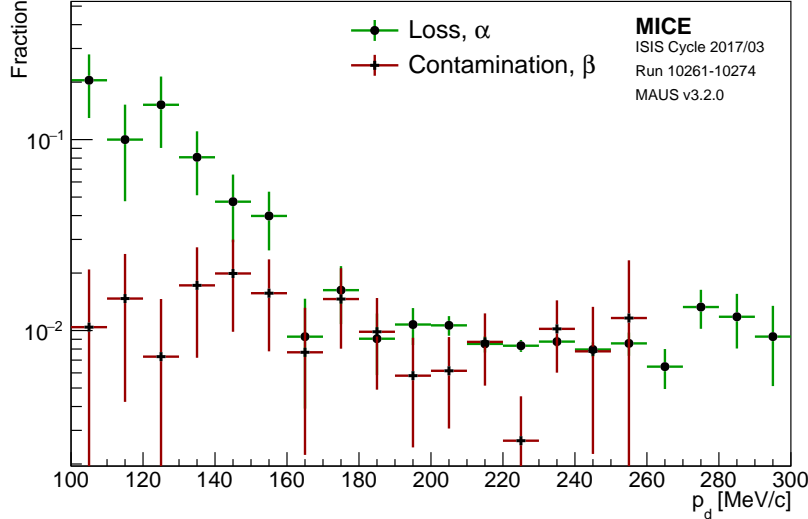


Figure 27: Percentage of electron contamination,  $\beta$ , and muon loss,  $\alpha$ , for different ranges of momentum measured in the downstream tracker,  $p_d$ . The error bars are based on the statistical uncertainty in a bin.

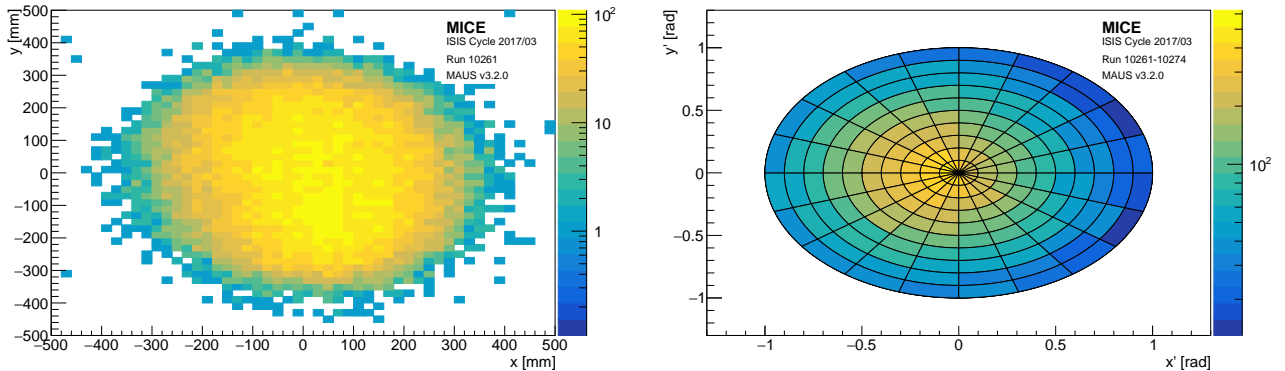


Figure 28: (Left) Beam profile at the entrance of the EMR. (Right) Polar plot of the track gradients in the EMR. The radial excursion represents the angle with respect to the  $z$  axis and the angle represents the azimuth.

In the muon hypothesis, the Continuously Slowing Down Approximation (CSDA) is used to estimate the muon momentum from its range in polystyrene, the active material of the detector. The range of a muon,  $\mathcal{R}$ , in the CSDA simply reads

$$\mathcal{R} = \int_{T_0}^0 \frac{dE}{|dE/dx|} = \int_{p_0}^0 \frac{dp}{|dE/dx|} \beta c, \quad (10)$$

with  $T_0$ ,  $p_0$  the kinetic energy and momentum of the impinging momentum and  $dE/dx$  the mean ionization energy loss. The impinging momentum,  $p_0$ , may be recovered by numerically inverting equation 10. The momentum reconstructed from the time-of-flight between TOF1 and TOF2,  $p_{12}$ , is propagated to the entrance of the EMR by subtracting the energy lost in TOF2 and the KL. This provides an estimate of  $p_0$  that may be used to validate the momentum reconstruction in the EMR, as shown in figure 30.

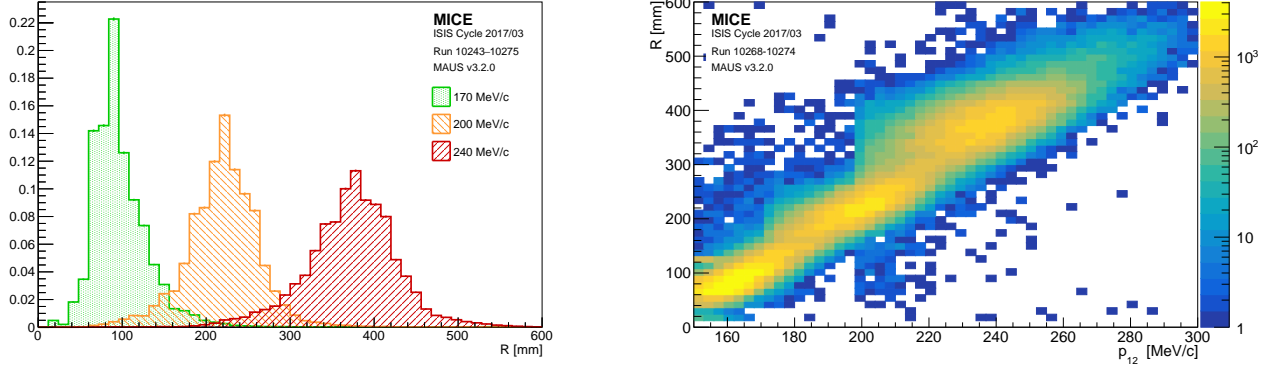


Figure 29: (Left) EMR range distributions of the data sets in the range 170–240 MeV/c. (Right) EMR range as a function of the momentum reconstructed from the time-of-flight between TOF1 and TOF2.

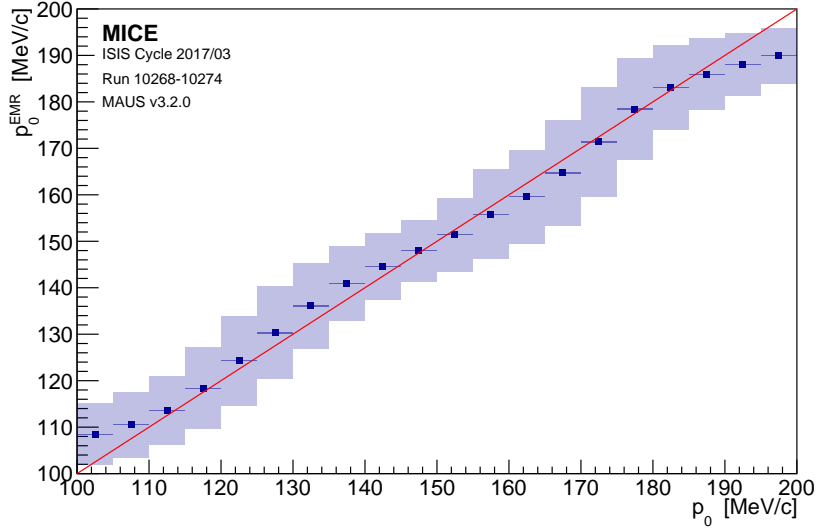


Figure 30: Momentum reconstructed in the EMR as a function of the momentum estimated at the entrance of the EMR from the time-of-flight information. The markers represent the mean in the bin, the dark band the uncertainty on the mean and the light band the RMS. The red line represents perfect agreement.

## 6 The Trackers

### 6.1 Introduction

MICE is equipped with two identical, high precision scintillating-fibre ("sciFi") trackers, described in [1]. Each tracker is placed in a superconducting solenoid designed to provide a uniform field over the tracking volume. One tracker, TKU, is upstream of the cooling cell, the other, TKD, downstream. Each tracker consists of five detector stations, labelled 1 to 5, with the stations placed varying distances apart to help resolve ambiguities. The trackers are placed symmetrically about the cooling cell, with station 1 the nearest to the cooling cell for both. Each station is formed of three planes of  $350\mu\text{m}$  scintillating-fibres, orientated at 120 degrees to one another. Each plane consists of two layers. The fibres in each plane butt up to each other and the two layers

are offset with respect to each other by a fibre radius. A charge particle will then deposit energy in at least 350 $\mu$ m of scintillator, providing uniform response over the whole station face. The doublet layers are glued to a sheet of mylar and the fibres are adjacent groups of seven fibres form one read-out channel. The three views are referred to as U, V and W, with the order being identical for each station and the U fibres running vertically. The light from the seven scintillating fibres passes into a single clear fibre, which takes it to a visible light photon counter (VLPC) which operate at 9k. The signal from the VLPCs is digitised using electronics developed by the D0 collaboration[2].

470

## 6.2 Tracker Performance and Reconstruction

475

### 6.2.1 Low Level Analysis

Low level analysis including digits, to spacepoints, 2 pages, Melissa U.

### 6.2.2 Noise

Noise at electronics level discussion, 1/2 page, Chris H and Noise from data, 1/2 page, Chris H

### 6.2.3 Track Finding Efficiency

480 Track selection/Kalman, efficiency (from all data runs plotted by pt and if all equal just 10mm can be shown)  
resolution (from MC), reference MAUS and Tracker SW paper, 1 page, Chris H.

485

### 6.2.4 Track Fit Predicted Performance

Monte Carlo simulation used with realistic field and beam conditions in order to estimate the reconstruction performance. Run number 09964 was used, representing a typical data set used for the study of emittance evolution.

## 6.3 Tracker Efficiency Evolution

Tracker efficiency with time (maybe 1 runs every 3 months since start shown?), 1/2 page, Paul K.

## 7 PID

### 7.1 Introduction

### 490 7.2 Performance of the PID

## 8 Track Matching

### 8.1 Global reconstruction

The overall detector performance can be validated by extrapolating tracks from one detector to another and comparing the reconstructed coordinates with the extrapolated values. Tracks measured in the upstream tracker 495 are extrapolated upstream to ToF1 and ToF0, and downstream to TKD and ToF2. Where there are materials in the beamline, the energy change on passing through the material is estimated using the most probable energy loss. Material thicknesses are approximated by the on-axis thickness.

Asymmetric effects can be introduced due to scattering from the walls of the cooling channel as the beam is not symmetric in the channel. In order to minimise the effects of such scattering, only events whose projected 500 trajectory is significantly distant from the apertures are considered in this analysis. The following sample selection is considered:

- Downstream sample: Events must be included in the downstream sample to be considered in this analysis
- Aperture cut: The projected upstream track must be within 100 mm radius from the beam axis at the 505 following apertures: the upstream absorber safety window; the upstream absorber window; the absorber centre; the downstream absorber window; the downstream absorber safety window; the upstream edge of SSD; the Helium window in SSD; the downstream edge of the downstream PRY aperture. This is performed even when the IH2 absorber was not installed, for the sake of consistency and because in some instances mounting flanges can limit the aperture and consistency.
- 1 space point in ToF2: The event must have exactly one space point in ToF2.
- Successful track extrapolation to ToF2: The projected upstream track must have been successfully 510 extrapolated to ToF2

The sample sizes are shown for data in table 5 and 6. The equivalent MC sample sizes are listed in 7 and 8.

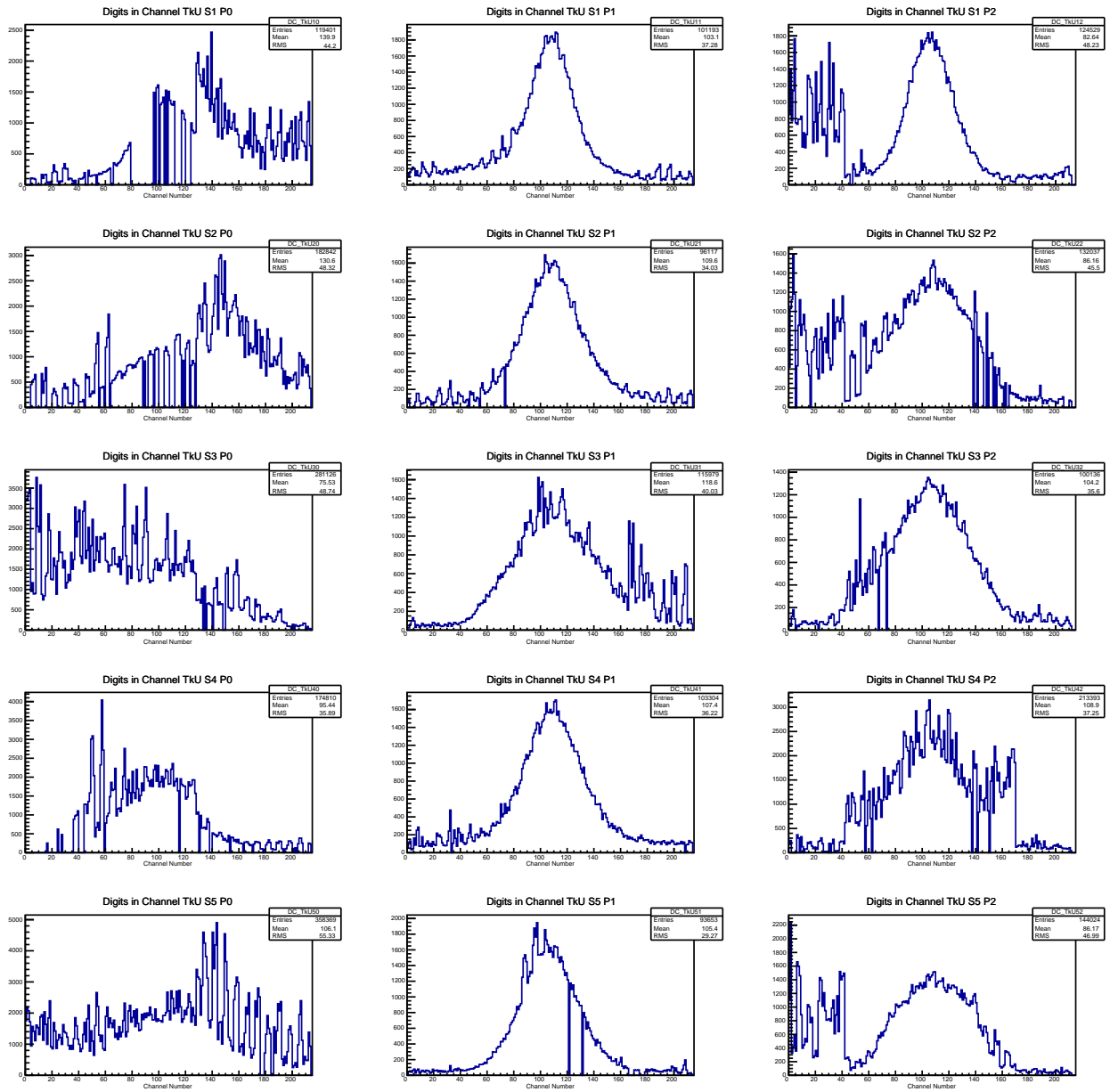


Figure 31:

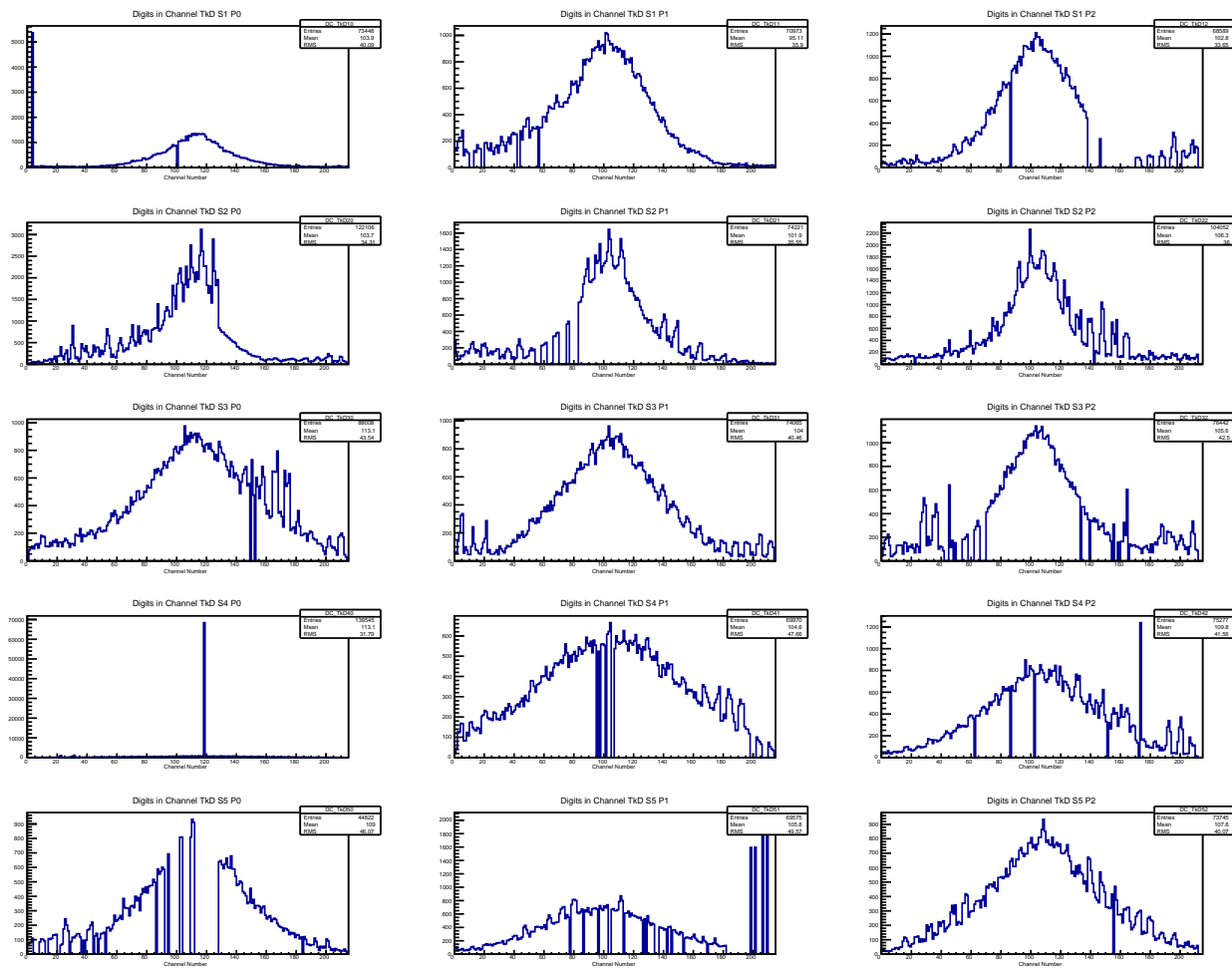


Figure 32:

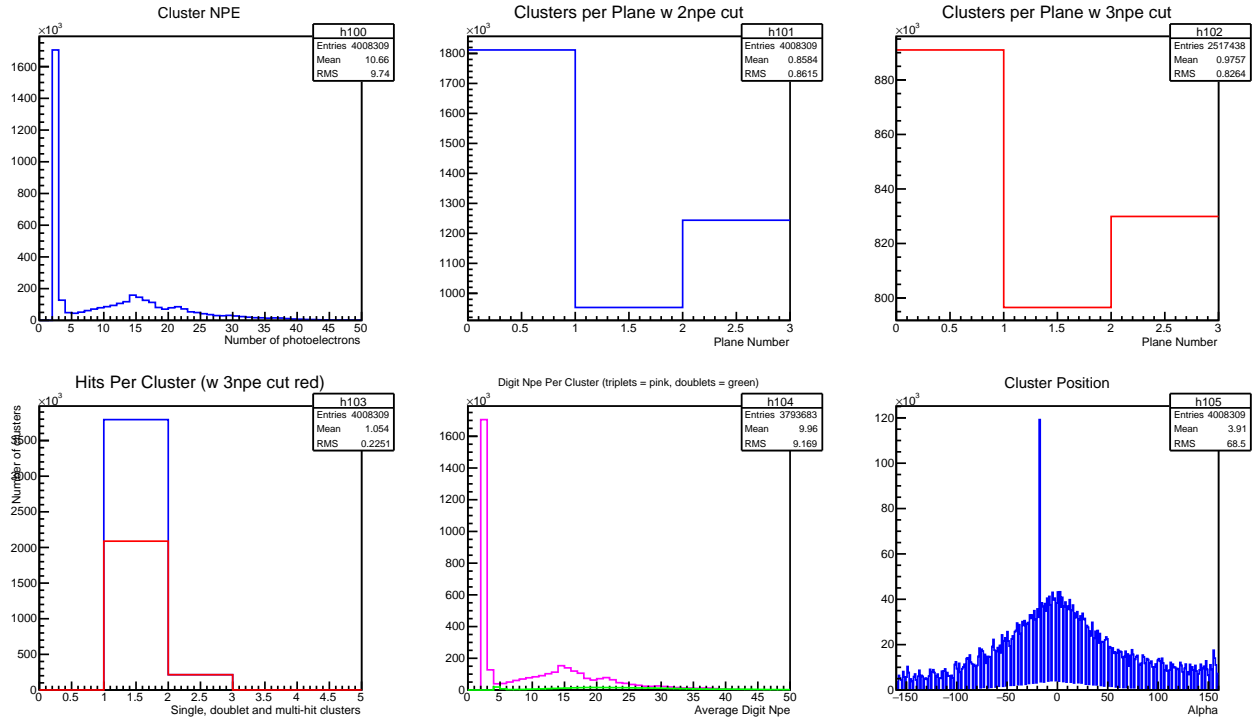


Figure 33:

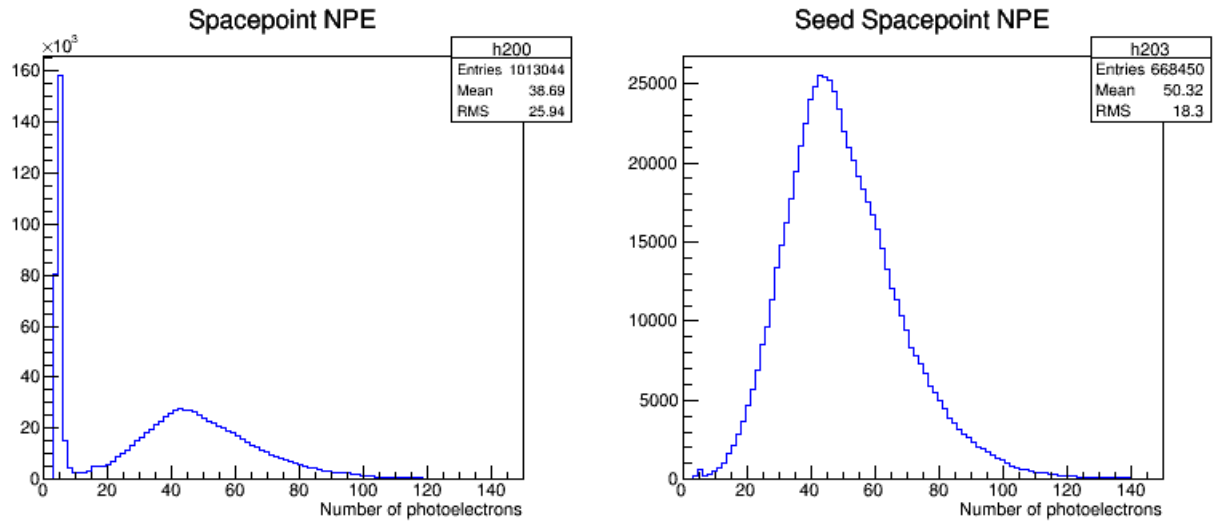


Figure 34: [left] The NPE of each spacepoint in the US and DS trackers combined. [Right] only the NPE of those spacepoints which go on to make tracks in the US and DS trackers combined are shown.

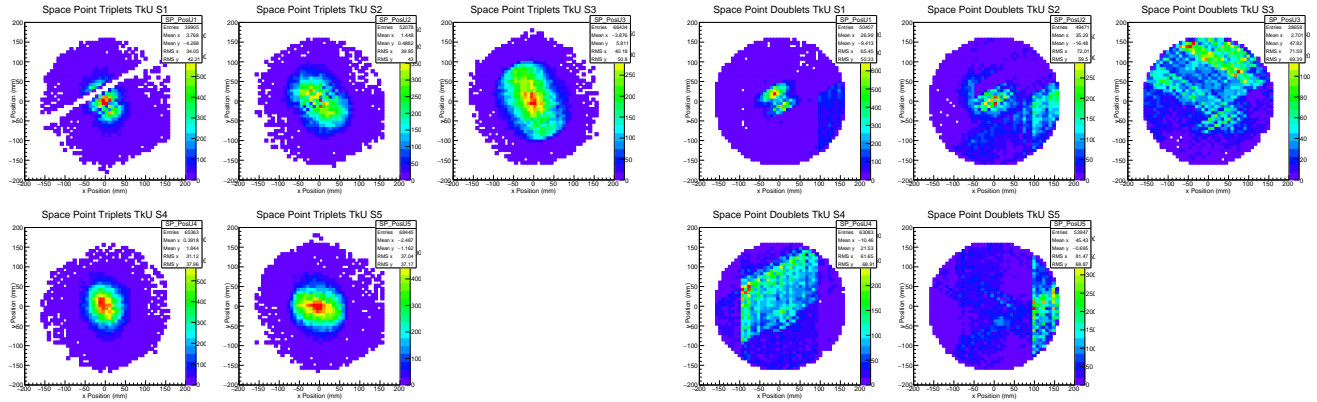


Figure 35:

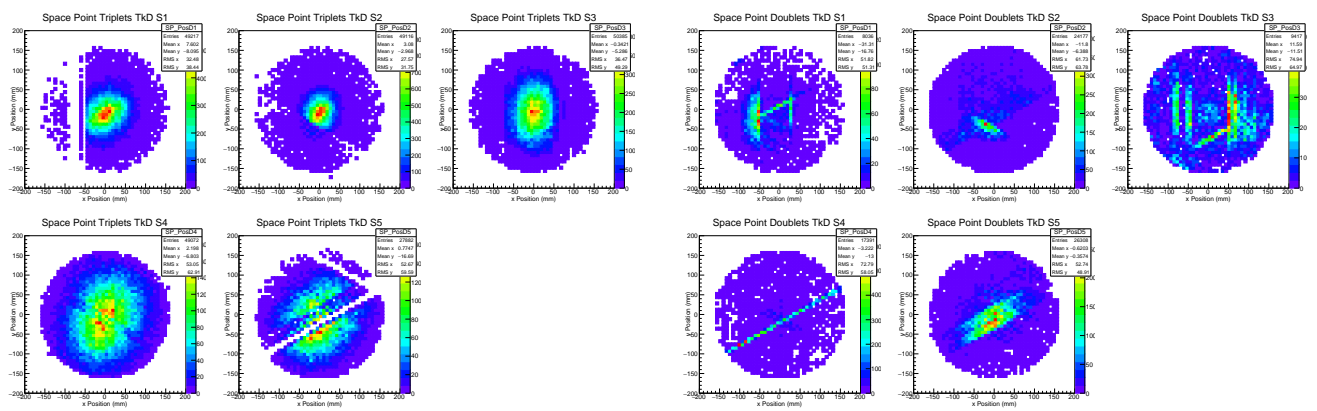


Figure 36:

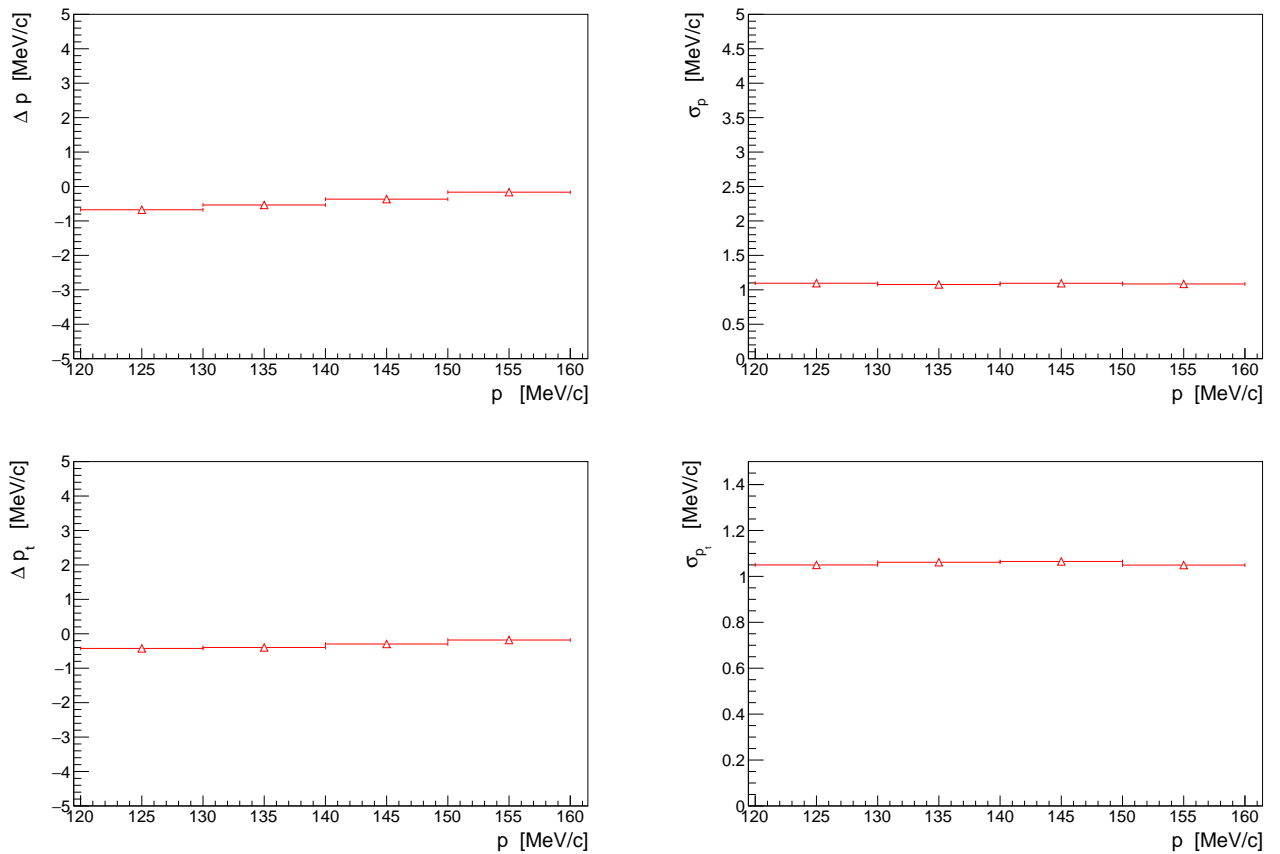


Figure 37: Predicted momentum reconstruction bias (left) and resolution (right) for the longitudinal (top) and transverse (bottom) momentum components in the upstream tracker.

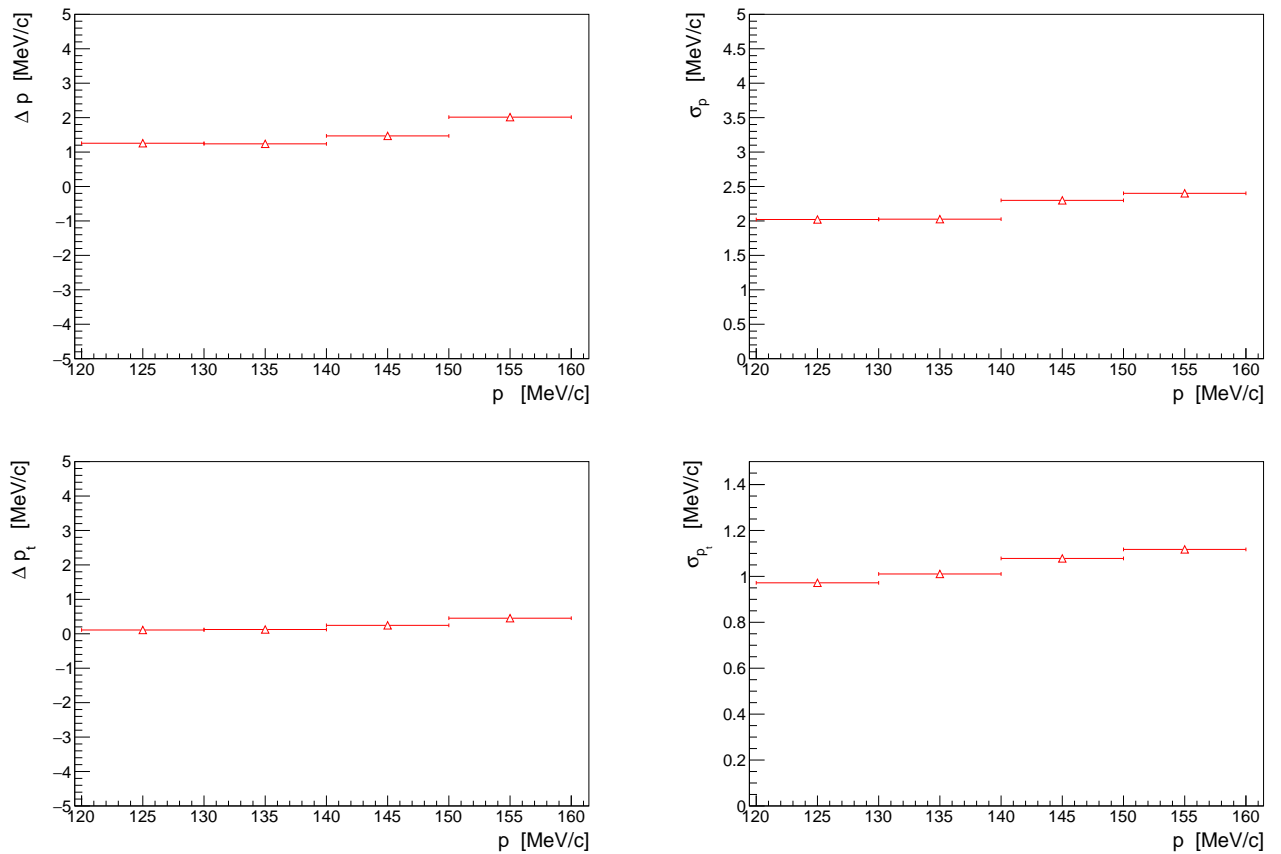


Figure 38: Predicted momentum reconstruction bias (left) and resolution (right) for the longitudinal (top) and transverse (bottom) momentum components in the downstream tracker.

Table 5: The extrapolated reconstructed data sample is listed. Samples are listed for 3-140 and 4-140 datasets.

	2017-2.7 3-140 None	2017-2.7 3-140 IH2 empty	2017-2.7 3-140 IH2 full	2017-2.7 3-140 LiH	2017-2.7 4-140 None	2017-2.7 4-140 IH2 empty	2017-2.7 4-140 IH2 full	2017-2.7 4-140 LiH
Downstream Sample	13019	8688	9058	11918	29712	23726	8407	24024
Cooling channel aperture cut	7203	4721	5166	6836	17731	14571	4935	14293
One space point in ToF2	6935	4506	4885	6477	16800	13817	4596	13362
Successful extrapolation to TKD	6935	4506	4885	6477	16800	13817	4596	13362
Successful extrapolation to ToF2	6935	4506	4885	6477	16800	13817	4596	13362
Extrapolation Sample	6935	4506	4885	6477	16800	13817	4596	13362

Table 6: The extrapolated reconstructed data sample is listed. Samples are listed for 6-140 and 10-140 datasets.

	2017-2.7 6-140 None	2017-2.7 6-140 IH2 empty	2017-2.7 6-140 IH2 full	2017-2.7 6-140 LiH	2017-2.7 10-140 None	2017-2.7 10-140 IH2 empty	2017-2.7 10-140 IH2 full	2017-2.7 10-140 LiH
Downstream Sample	27025	17783	29577	31257	14847	7278	14784	17138
Cooling channel aperture cut	15238	10129	16045	17122	5633	2837	5057	6075
One space point in ToF2	14432	9479	14826	15774	5276	2614	4471	5372
Successful extrapolation to TKD	14432	9479	14826	15774	5276	2614	4471	5372
Successful extrapolation to ToF2	14432	9479	14826	15774	5276	2614	4471	5372
Extrapolation Sample	14432	9479	14826	15774	5276	2614	4471	5372

Table 7: The extrapolated reconstructed simulated sample is listed. Samples are listed for 3-140 and 4-140 datasets.

	Simulated 2017-2.7 3-140 None	Simulated 2017-2.7 3-140 IH2 empty	Simulated 2017-2.7 3-140 IH2 full	Simulated 2017-2.7 3-140 LiH	Simulated 2017-2.7 4-140 None	Simulated 2017-2.7 4-140 IH2 empty	Simulated 2017-2.7 4-140 IH2 full	Simulated 2017-2.7 4-140 LiH
Downstream Sample	8585	8567	8511	8624	18247	18247	18455	18553
Cooling channel aperture cut	5112	4715	5032	5378	10884	10997	10758	10404
One space point in ToF2	4540	4184	4499	4820	9544	9747	9467	9117
Successful extrapolation to TKD	4540	4184	4499	4820	9544	9747	9467	9117
Successful extrapolation to ToF2	4540	4184	4499	4820	9544	9747	9467	9117
Extrapolation Sample	4540	4184	4499	4820	9544	9747	9467	9117

Table 8: The extrapolated reconstructed simulated sample is listed. Samples are listed for 6-140 and 10-140 datasets.

	Simulated 2017-2.7 6-140 None	Simulated 2017-2.7 6-140 IH2 empty	Simulated 2017-2.7 6-140 IH2 full	Simulated 2017-2.7 6-140 LiH	Simulated 2017-2.7 10-140 None	Simulated 2017-2.7 10-140 IH2 empty	Simulated 2017-2.7 10-140 IH2 full	Simulated 2017-2.7 10-140 LiH
Downstream Sample	17810	18031	18188	18259	8843	9029	9155	9294
Cooling channel aperture cut	10289	10071	9449	9906	3424	3393	3227	3337
One space point in ToF2	9014	8766	8219	8577	2941	2926	2772	2861
Successful extrapolation to TKD	9014	8766	8219	8577	2941	2926	2772	2861
Successful extrapolation to ToF2	9014	8766	8219	8577	2941	2926	2772	2861
Extrapolation Sample	9014	8766	8219	8577	2941	2926	2772	2861

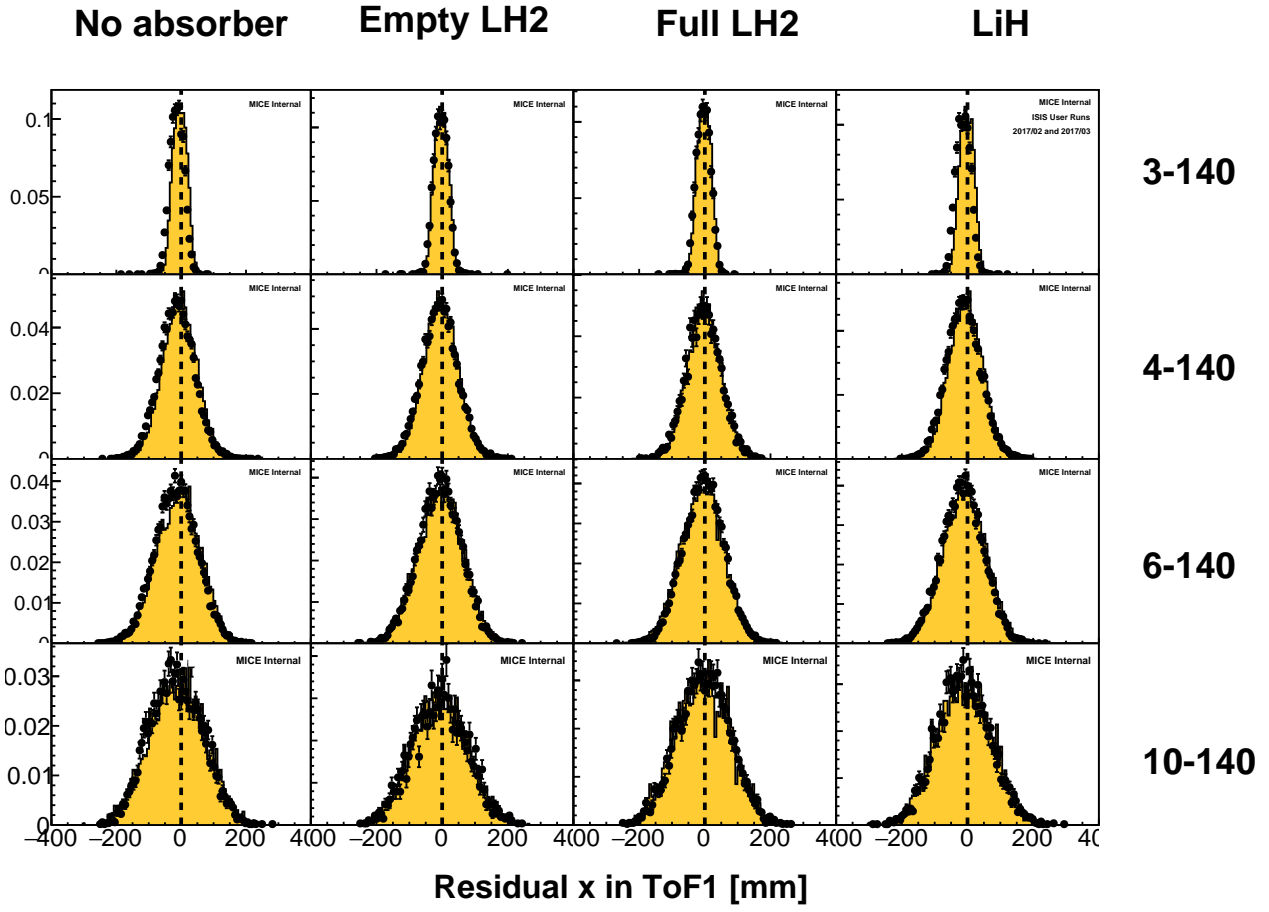


Figure 39: Residual horizontal (x) position in ToF1 of tracker tracks following extrapolation from TKU.

The extrapolated position following extrapolation to ToF1 is shown in fig. 39 and 40. In general the width of the distributions are comparable between MC and data. Where the diffuser is in place for higher emittance beams, the extrapolation goes through the diffuser material so the residuals are wider, owing to the increased scattering from the diffuser.  
515

The time-of-flight residual in data shows a systematic offset from 0 and relative to the MC. The offset from 0 gets worse for higher emittance beams. It is thought to be an intrinsic property of the beam; muons that are scattered in materials between the tracker and the TOF have systematically shorter path lengths than the 520 extrapolated trajectories, resulting in systematically longer extrapolated time of flight. The MC reconstruction is known to have issues, as evidenced by the discrepancy in slab  $dt$  for ToF0 and ToF1.

#### Plot momentum vs $dt$ for ToF01 and ToF12

Small misalignments between TKU extrapolated tracks and TKD are observed, indicated by the offset of transverse variables from 0, shown in fig. 42 and 43. There are known, uncorrected misalignments in the 525 detector system and there are expected to be additional misalignments in the magnets which could lead to these offsets.

The total momentum shows discrepancy between TKU and TKD of about 1 MeV/c. This is consistent with the systematic offset in the tracker momentum resolution shown in fig. ?? and ???. It is interesting to note that the level of agreement between MC and data varies on a setting-by-setting basis in a statistically significant manner. Agreement is better for the settings where the liquid hydrogen windows were installed.  
530

Further small misalignments are observed in the position residuals between TOF2 and tracks extrapolated

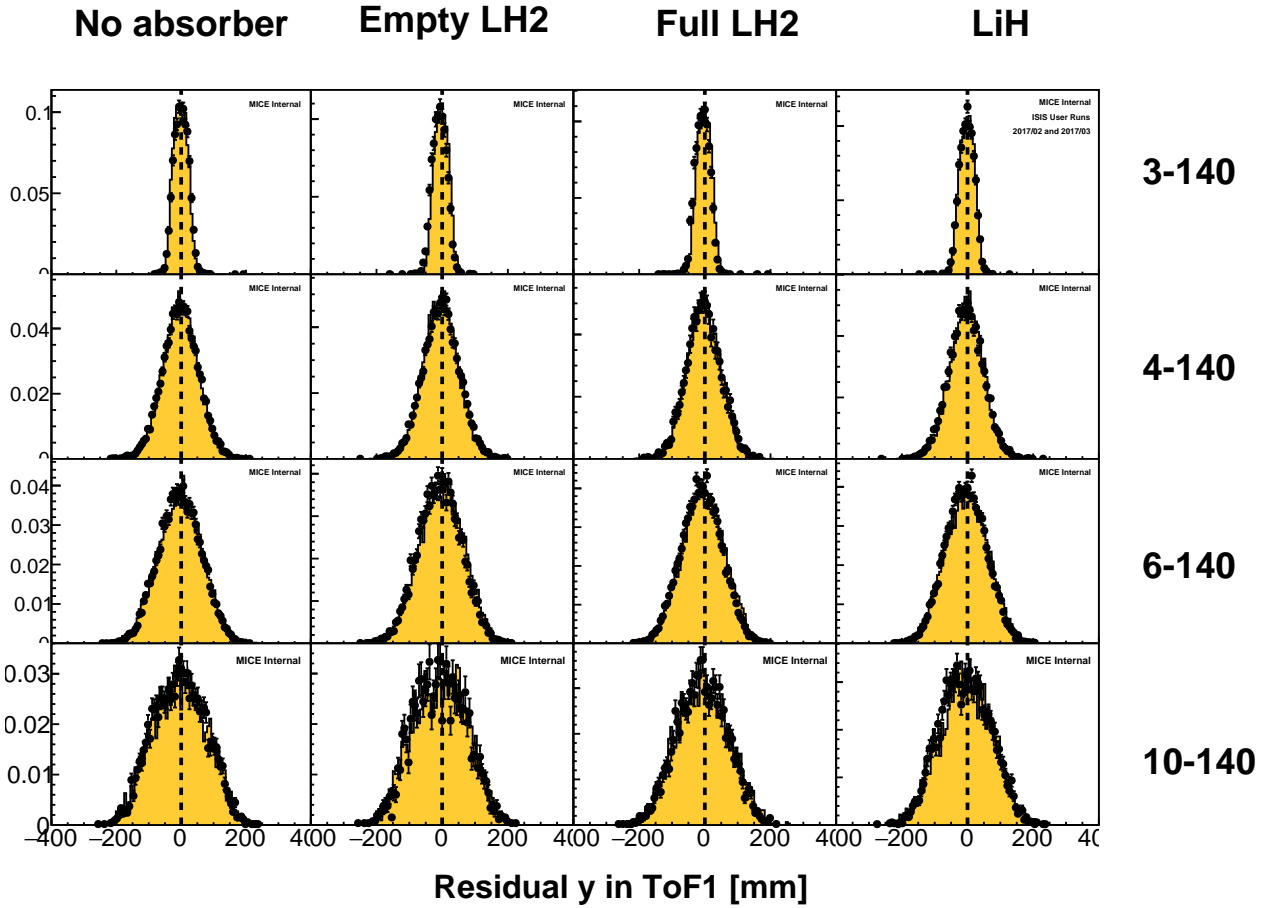


Figure 40: Residual vertical (y) position in ToF1 of tracker tracks following extrapolation from TKU.

from TKD. This is attributed to alignment issues.

TOF2 exhibits a significant offset from the extrapolated track.

## 8.2 Beam based magnet alignment

## 535 9 Beam-based detector alignment

To carry out its program, MICE requires all of its detectors to reconstruct space points in a globally consistent fashion. A beam-based alignment algorithm was developed to improve the resolution on the position of the scintillating-fibre trackers lodged inside the bores of superconducting magnets. This method can achieve unbiased measurements of the trackers rotation angles with a resolution of  $6 \text{ mrad}/\sqrt{N}$  and of their position with a resolution of  $20 \text{ mm}/\sqrt{N}$ , with  $N$  the number of selected tracks. This section briefly describes the alignment algorithm and presents the results obtained during the 2017/01 ISIS user cycle as an example case. The procedure is described in greater details and cross-checked on several simulations in [17].

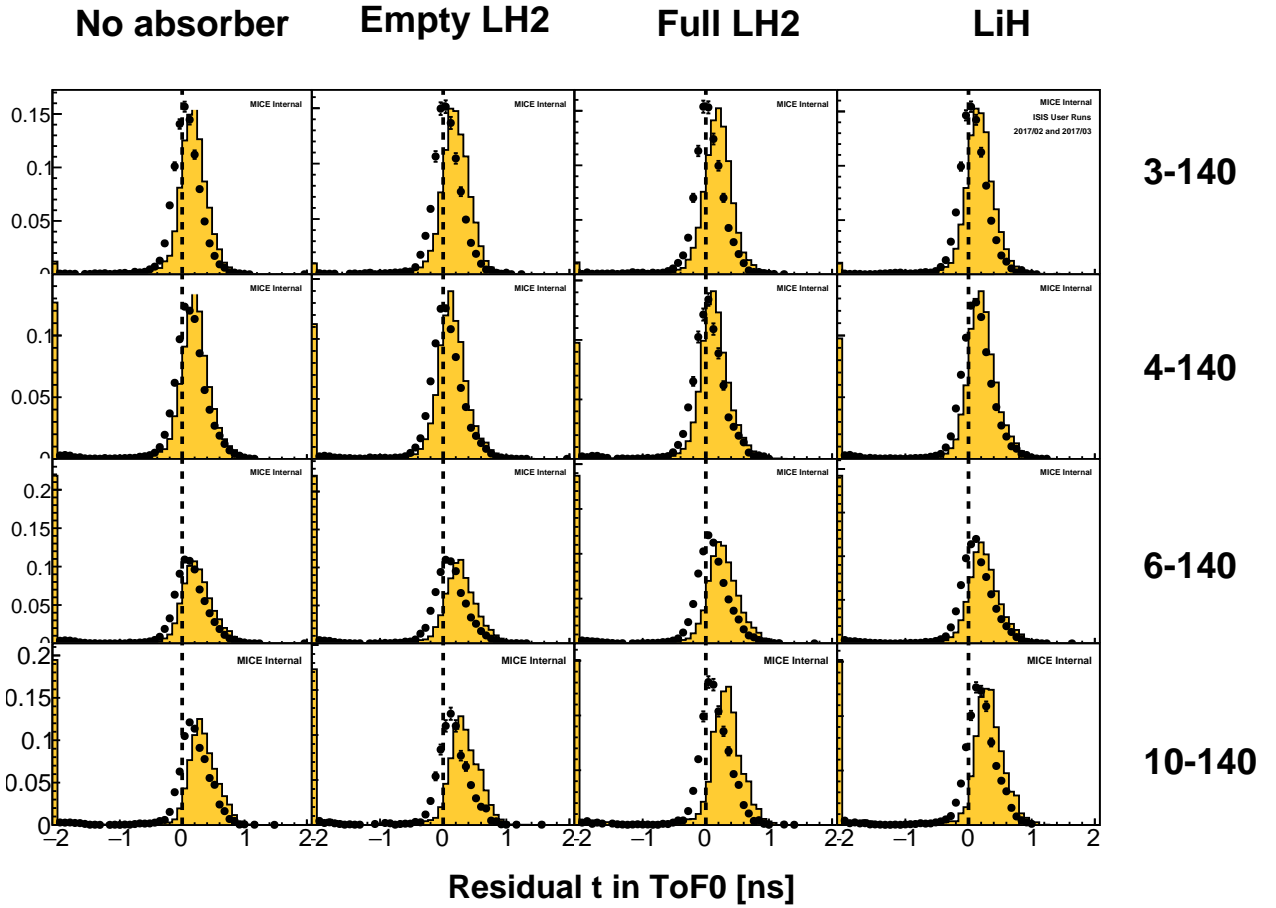


Figure 41: Residual ToF0 time of the extrapolated track. Track trajectories were drawn from TKU, while the track times were drawn from ToF1 with appropriate offsets for time-of-flight from TKU to ToF1 considered.

## 9.1 Introduction

The single-particle nature of the MICE experiment requires reliable global track matching throughout, i.e. the ability to associate a trace measured in the upstream tracker with one in the downstream tracker but also with the particle identification detectors. The many detectors must reconstruct space points in a globally consistent fashion to guarantee reliable and efficient track matching, as well as unbiased muon scattering measurements.

The baseline for the beam-based alignment is the surveys of the detectors in the hall using laser telemetry. Surveys were performed regularly throughout the MICE Step IV commissioning phase and data taking period. The TOF1 time-of-flight hodoscope was moved periodically to access the upstream end of the superconducting solenoids and resurveyed systematically. The downstream particle identification detectors module, composed of TOF2, the KL and the EMR, was also repositioned on occasion. The focus coil module was moved in and out of the beam line to change absorbers. Each of these events was followed by a complete resurvey.

The particle identification detectors are each equipped with at least four survey monuments and are surveyed directly. The two scintillating fibre trackers, nested in the superconducting solenoids, can not be accessed. The upstream and downstream flanges of each solenoid are surveyed and the end plate of the trackers are surveyed with respect to the flanges. The estimated position of the trackers within the bores are inferred from these measurements. A laser theodolite is used to locate the monuments with respect to the datum point situated under

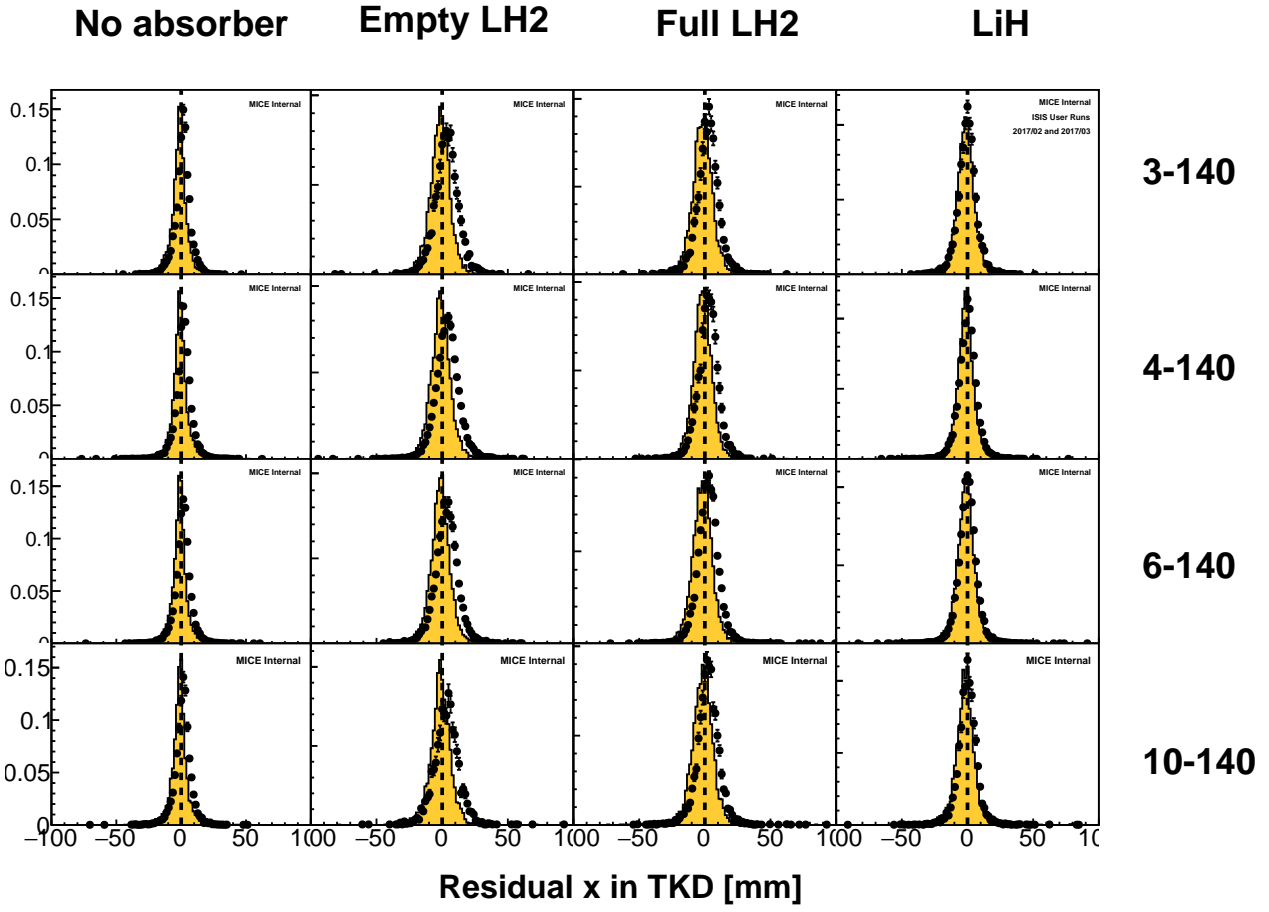


Figure 42: Residual  $x$  position of TKU tracks extrapolated to TKD, as compared to the tracks in TKD.

the second dipole magnet, D2. Figure 50 shows a picture of TOF2 and the location of its survey monuments.

Before being placed inside the magnets, each tracker was surveyed independently using a coordinate-measuring machine (CMM). This ensures that the position of the five stations is well known within each tracker with respect to the end plate. Figure 51 shows the disposition of the stations in the downstream scintillating fibre tracker and their position as measured by the CMM. The reference position is the axis that joins the centre of station 1 to the centre of station 5. The positions of stations 1 to 3 are measured with respect to that axis. The beam can be used to check the tracker station alignment.

Special care is taken during the installation of the trackers within the magnet bores. The installation platform is adjustable to enable the tracker to be aligned with the bore of the solenoid. The tracker sits on four adjustable feet, two at each end. The adjustable feet are used to align the tracker with the magnetic axis of the solenoid. Once this has been done, the location bracket is fitted. The location bracket locks the tracker in its longitudinal and azimuthal positions.

## 9.2 Analysis method

The position of tracker  $t = u, d$  in global coordinates is entirely defined by the location of its centre ( $x_T, y_T, z_T$ ) and a set of Tait-Bryan angles ( $\alpha_T, \beta_T, \gamma_T$ ). The  $z$  axis is oriented along the beam line and points downstream, the  $y$  axis points upwards and the  $x$  axis completes the right-handed coordinate system. The rotation about

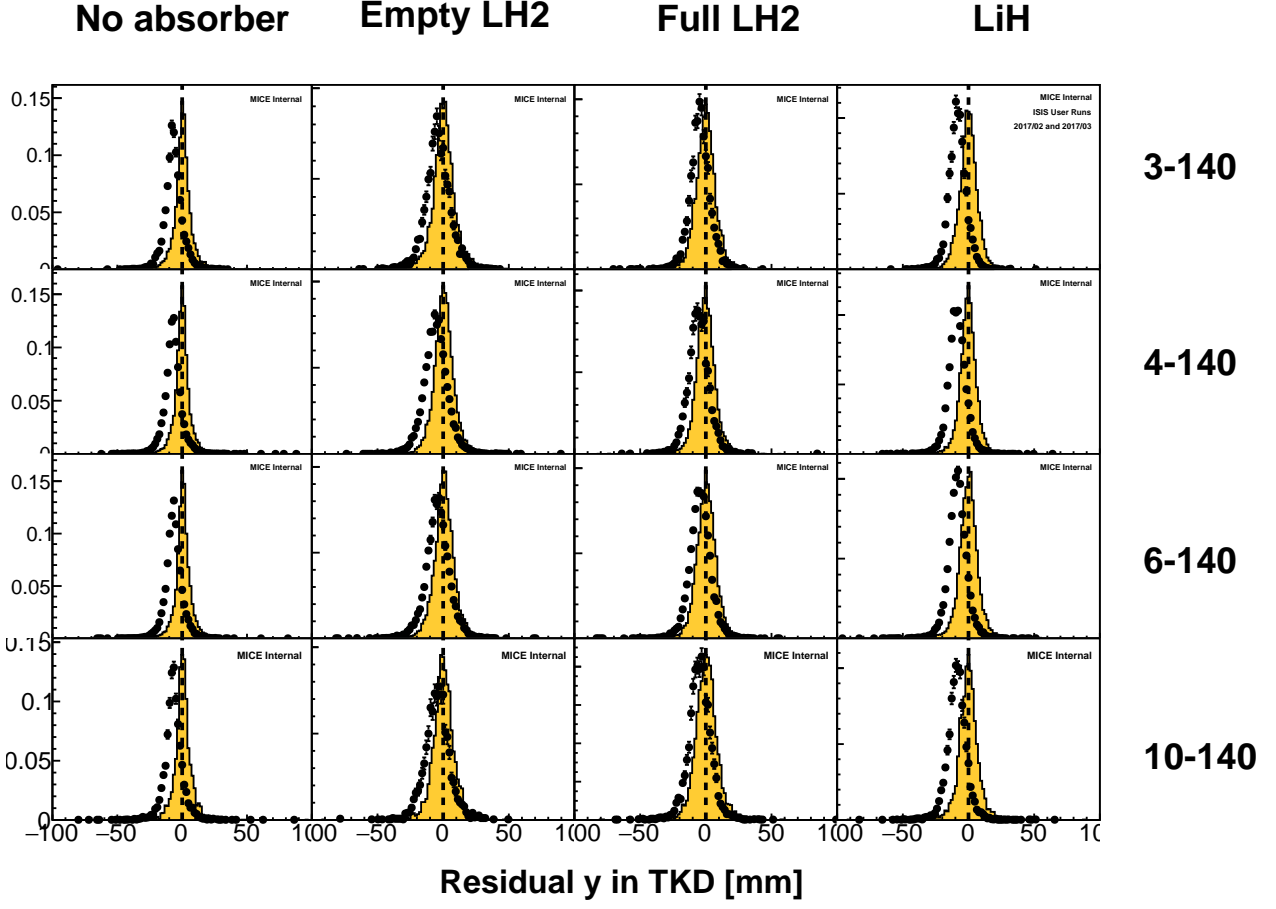


Figure 43: Residual  $y$  position of TKU tracks extrapolated to TKD, as compared to the tracks in TKD.

$x$ ,  $\alpha_T$ , is called pitch, about  $y$ ,  $\beta_T$ , is called yaw and about  $z$ ,  $\gamma_T$ , is called roll. For a straight track of local coordinates  $(x_t, y_t, z_t)$  at the tracker centre, the global coordinates are reconstructed as

$$\begin{pmatrix} \xi_t \\ v_t \\ \zeta_t \end{pmatrix} = \begin{pmatrix} x_t - \gamma_T y_t + \beta_T z_t + x_T \\ y_t + \gamma_T x_t - \alpha_T z_t + y_T \\ z_t - \beta_T x_t + \alpha_T y_t + z_T \end{pmatrix}. \quad (11)$$

in the first order small angles approximation. The global gradients of the straight track thus read

$$\begin{aligned} \xi'_t &= \frac{d\xi_t}{d\zeta_t} = \frac{dx_t - \gamma_T dy_t + \beta_T dz_t}{dz_t (1 - \beta_T x'_t + \alpha_T y'_t)} \simeq x'_t - \gamma_T y'_t + \beta_T, \\ v'_t &= \frac{dv_t}{d\zeta_t} = \frac{dy_t + \gamma_T dx_t - \alpha_T dz_t}{dz_t (1 - \beta_T x'_t + \alpha_T y'_t)} \simeq y'_t + \gamma_T x'_t - \alpha_T. \end{aligned} \quad (12)$$

There are six potential unknowns per tracker. Some simplifications can be made to lower the amount of unknowns. The  $z_T$  coordinate of each tracker is known to great accuracy from the survey. It may also be shown that the roll of the trackers has negligible influence on the alignment and may be ignored [17]. The beam-based detector alignment is critical to find the  $(x_T, y_T, \alpha_T, \beta_T)$  constants for each tracker.

The location of the TOFs is used as the reference for the tracker alignment. The line that joins the centre of TOF1 with the centre of TOF2 is chosen to be the reference axis. A deviation from this axis is considered as a misalignment of the trackers. Multiple scattering in the beam line does not allow to do the alignment on single

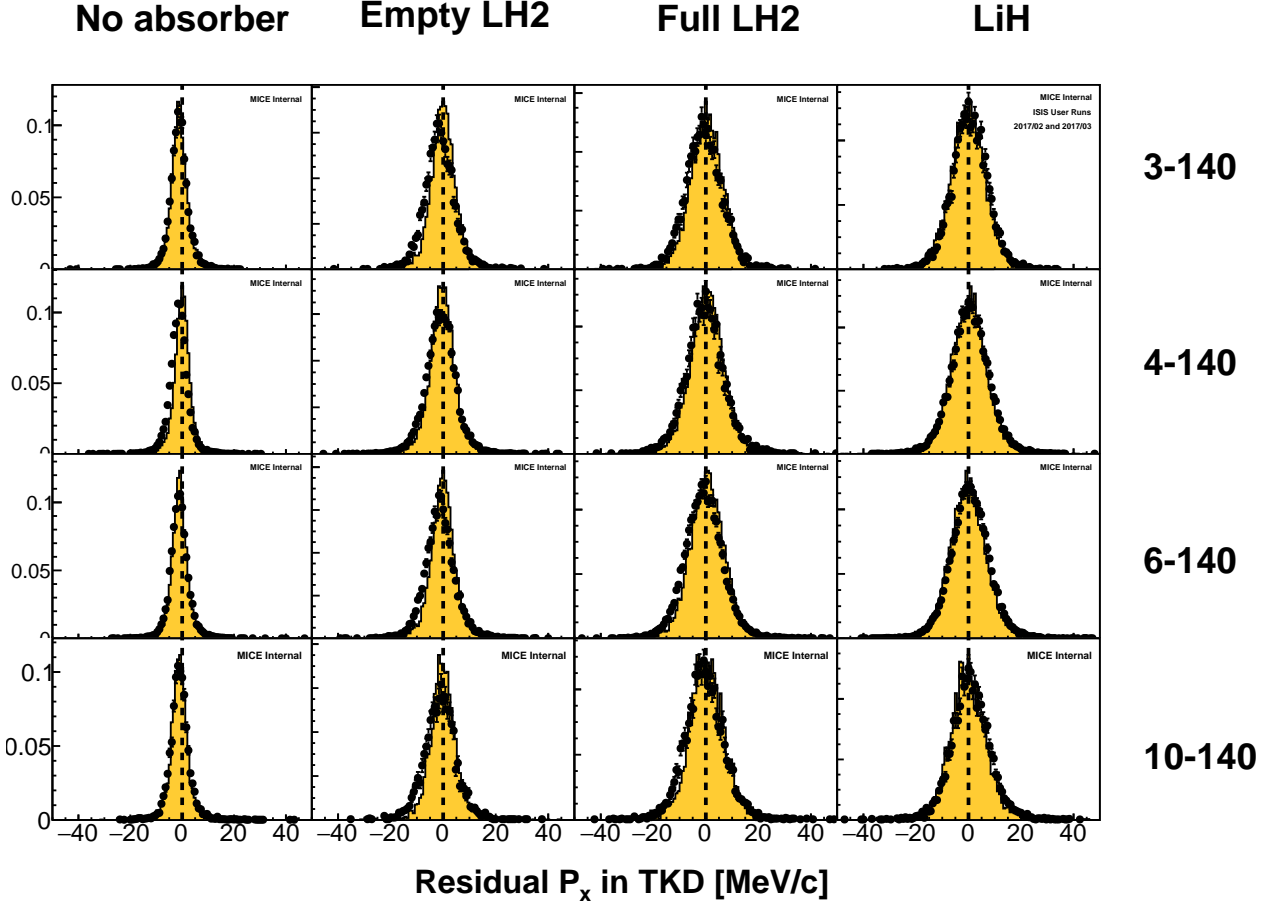


Figure 44: Residual  $p_x$  of TKU tracks extrapolated to TKD, as compared to the tracks in TKD.

particle basis but works for a larger sample of particles. The mean residual angles and positions of the trackers  
580 with respect to the TOF12 axis are an essential and powerful tool to infer the correction factors. Figure ?? shows the path of a single particle that scatters in the absorber module of the MICE experiment.

Each TOF provides a single space point in the global coordinate system  $(\xi_i, v_i, \zeta_i)$  with  $i$  the ID of the TOF. This position is assumed to be the true position with a large uncertainty due to the limited granularity of the detector ( $\sigma_x \sim \sigma_y \sim 17$  mm). The gradients of the track between the two TOFs are reconstructed as:

$$\psi'_{12} = \frac{\psi_2 - \psi_1}{\zeta_2 - \zeta_1}, \quad \psi = \xi, v. \quad (13)$$

The extrapolated position of the TOF reference track in the centre of tracker  $t = u, d$  is

$$\psi_{12}^t = \psi_1 + \frac{\psi_2 - \psi_1}{\zeta_2 - \zeta_1} (\zeta_T - \zeta_1) = (1 - \chi_T)\psi_1 + \chi_T\psi_2, \quad \psi = \xi, v, \quad (14)$$

with  $\chi_T = (\zeta_T - \zeta_1)/(\zeta_2 - \zeta_1)$ , the fractional distance from TOF1 to the tracker centre.

Tracker  $t = u, d$  samples the particle track in five different stations  $(x_t^j, y_t^j, z_t^j)$ , with  $j = 1, \dots, 5$ . This allows for the reconstruction of a straight track with gradients  $x'_t$  (resp.  $y'_t$ ) in the  $xz$  (resp.  $yz$ ) projection and 585 its position at the centre,  $(x_t, y_t, 0)$ . No assumption is made on the prior position of the tracker and hence the coordinates and gradients are returned in local coordinates, i.e. assuming a tracker perfectly aligned with the beam axis, whose centre lies at  $z = 0$ .

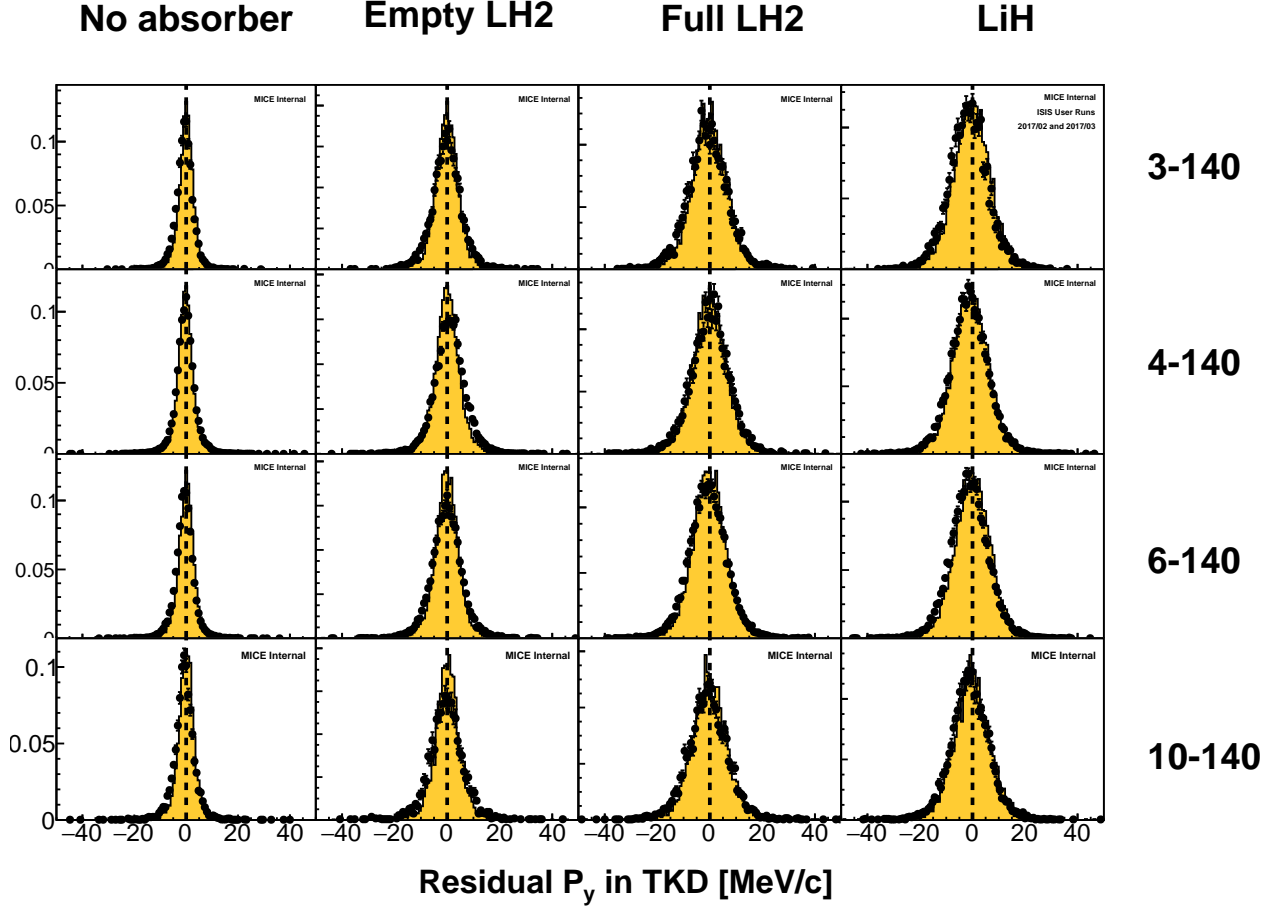


Figure 45: Residual  $p_y$  of TKU tracks extrapolated to TKD, as compared to the tracks in TKD.

In global coordinates, on average, the track reconstructed between TOF1 and TOF2 should agree with the track reconstructed in either tracker, i.e. the mean residuals should be zero. Applying this reasoning to the unknown offset and angles yields the following system of four equations with four unknowns [17]:

$$\begin{cases} \langle x'_t - \xi'_{12} \rangle = -\beta_T \\ \langle y'_t - v'_{12} \rangle = \alpha_T \\ \langle x_t - \xi^t_{12} \rangle = -x_T \\ \langle y_t - v^t_{12} \rangle = -y_T \end{cases}. \quad (15)$$

The measurement of four residual distributions per tracker yields the alignment constants.

The method described here assumes that the mean residuals can be measured with great accuracy and, more importantly, are unbiased. A bias in one of the residual distributions inevitably introduces a bias in the measurement of the corresponding alignment parameter, as they are directly proportional. The main source of bias is the scattering in the material between TOF1 and TOF2. If the beam is not perfectly centred, particles preferentially scrape out on one side of the magnet bore, anisotropically curbing a specific tail of the residual distribution. To nullify this effect, a fiducial cut is applied to the upstream sample. Only particles that are expected to be contained in the downstream tracker are included in the analysis [17].

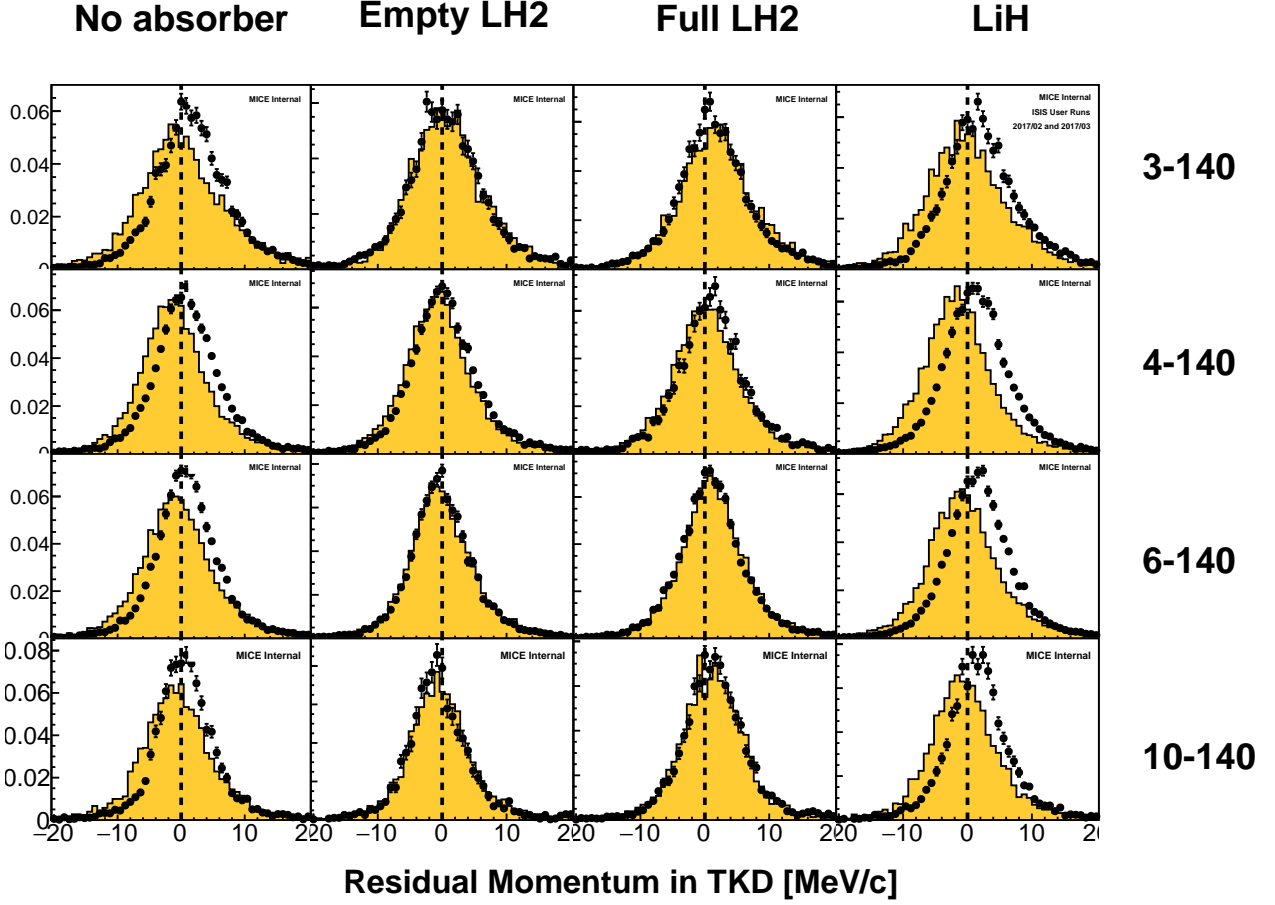


Figure 46: Residual  $p_{tot}$  of TKU tracks extrapolated to TKD, as compared to the tracks in TKD.

### 9.3 Alignment of a data sample

Data is recorded with the superconducting magnetic channel of the experiment turned off, i.e. with tracks going in a straight line from TOF1 to the beam dump. High momentum beams are used in order to reduce the RMS scattering angle and maximize transmission. The settings used correspond to ‘pion’ beams of positive polarity to maximize statistics. The beams exhibit a variety of distributions in the beam line. An agreement between the independent fits guarantees an unbiased measurement of the alignment constants.

Provided with the unbiased sample produced as described in section 9.2, each track yields a set of global gradients between TOF1 and TOF2,  $\xi'_{12}$  and  $v'_{12}$ , and global extrapolated positions at the tracker centres,  $\xi^t_{12}$  and  $v^t_{12}$ . It also records the position of the track at the centre of the trackers in local coordinates,  $x_t$  and  $y_t$ , and its local gradients,  $x'_t$  and  $y'_t$ . The residual distributions necessary to measure the left hand side of equations 15 are produced in order to measure the eight alignment parameters. Figure 53 shows the gradient residuals between  $y'_u$  and  $v'_{12}$  for run 9367. The mean residual yields the the pitch of the upstream tracker,  $\alpha_U$ .

To ensure the best possible fit to the tracker parameters, the algorithm is applied multiple times. The first estimate of  $x_T, y_T, \alpha_T, \beta_T$  is used as an input to the sample selection part of the algorithm. The process is repeated until the alignment constants converge. Figure 54 shows the evolution of the optimal upstream tracker pitch,  $\alpha_U^*$ , over five iterations for run 9367.

Each data set was processed independently with the algorithm. Figure 55 compiles the alignment parameters

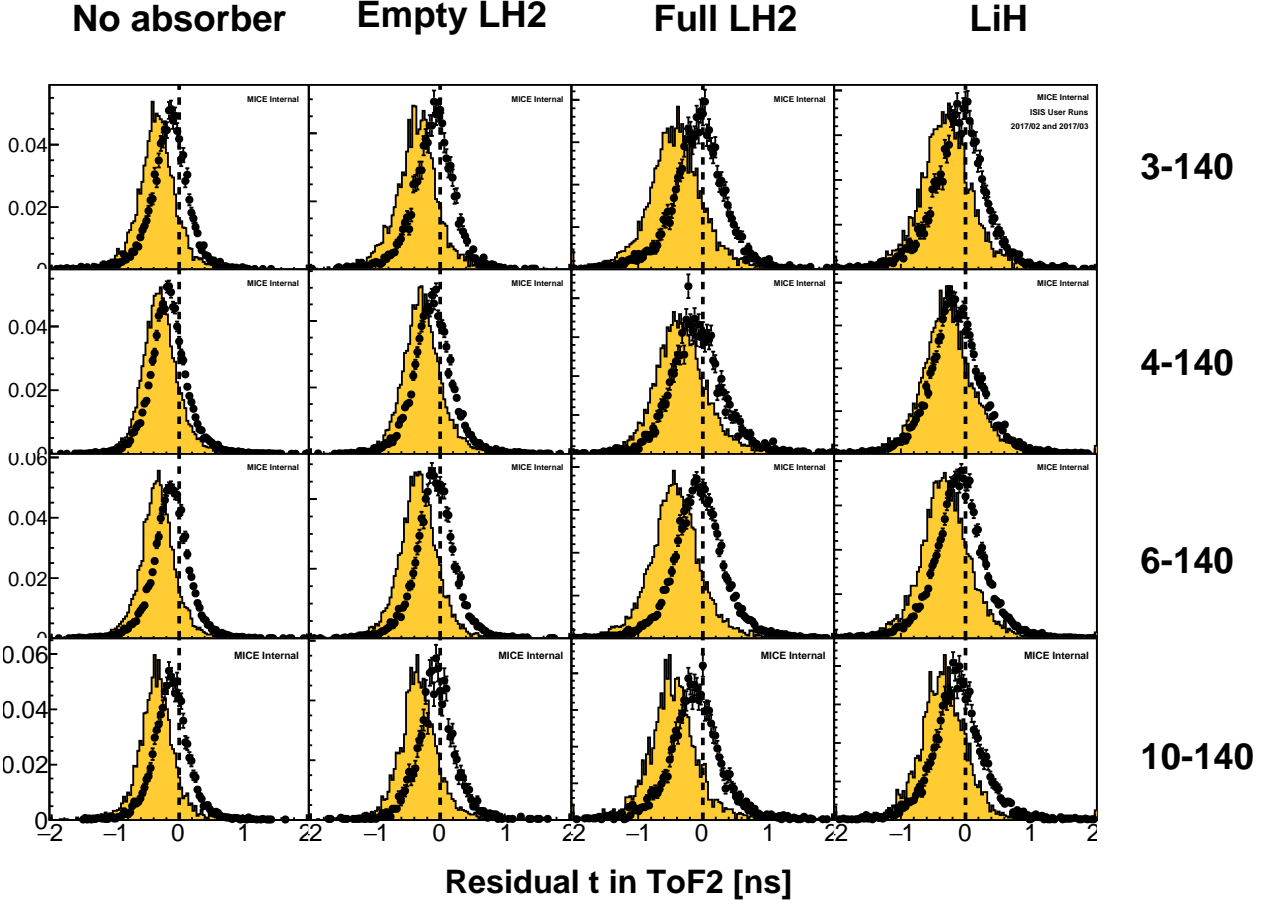


Figure 47: Residual time of TKU tracks extrapolated to ToF2, as compared to the time measured in ToF2. The track times were drawn from ToF1 with appropriate offsets for time-of-flight from TKU to ToF1 considered.

measured for each run. The measurements are in good agreement with one another and show no significant discrepancy. The constant fit  $\chi^2/\text{ndf}$  is close to unity for each fit, which indicates that there are no significant additional source of uncertainty. The optimal parameters are summarised in table 9.

	x [mm]	y [mm]	$\alpha$ [mrad]	$\beta$ [mrad]
TKU	$-0.032 \pm 0.094$	$-1.538 \pm 0.095$	$3.382 \pm 0.030$	$0.412 \pm 0.029$
TKD	$-2.958 \pm 0.095$	$2.921 \pm 0.096$	$-0.036 \pm 0.030$	$1.333 \pm 0.030$

Table 9: Summary table of the optimal alignment constants measured in the high-momentum straight-track data acquired during the 2017/01 ISIS user cycle.

## 9.4 Propagation

The fitted parameters are used to yield the global track coordinates at the tracker  $t = u, d$  centres,  $(\xi_t, v_t, \zeta_t)$ , through equation 11 and the global gradients  $\xi'_t, v'_t$  through equation 12. A corrected global track is propagated in an adjacent detector module  $M$  at  $\zeta_m$  through

$$\psi_t^m = \psi_t + \psi'_t(\zeta_m - \zeta_t), \quad \psi = \xi, v. \quad (16)$$

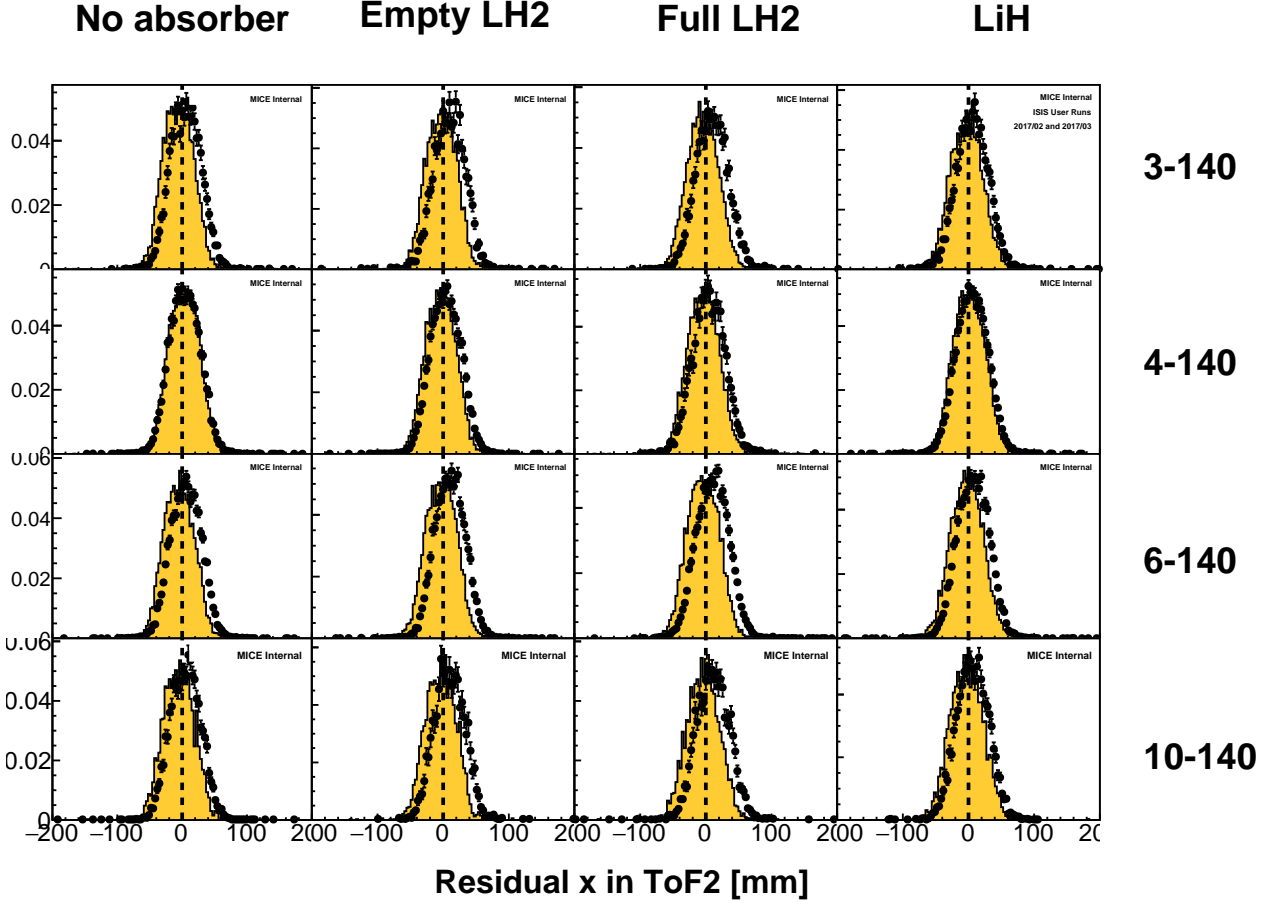


Figure 48: Residual  $x$  position of TKD tracks extrapolated to TOF2, as compared to the position measured in TOF2.

Provided exact corrections, a detector module  $M$  that measures a global position  $(\xi_m, v_m, \zeta_m)$  verifies

$$\begin{cases} \langle \psi_m - \psi_t^m \rangle = 0 \\ \langle \psi'_m - \psi'_t \rangle = 0 \end{cases}, \quad \psi = \xi, v. \quad (17)$$

As a consistency check, the tracks are first propagated between the two trackers. The results are shown in figure 56. The top left and right distributions show the residuals between the TKU and TKD tracks at the centre of the downstream tracker and at the level of the absorber, respectively. The bottom two histograms show the agreement between the angles measured upstream and downstream. The azimuthal angle residuals show consistency between the roll of the two trackers.  
620

The upstream tracker tracks are extrapolated into TOF1 and the downstream tracker tracks are propagated into the three downstream particle identification detectors: TOF2, the KL and the EMR. The residual plots are represented in figure 57. The values obtained show good agreement between the tracks and the space points measured in other MICE detectors.  
625

Special care is taken when evaluating the central value of the residual distributions. The two trackers and the Electron-Muon Ranger have a sufficient spacial resolution to follow a near-Gaussian distribution. The residuals involving these detectors are fitted with a standard multivariate normal of mean  $\mu$  and width  $\sigma$  between the two half-maximum, i.e. in the range  $\mu \pm 1.1775 \sigma$ . The TOF hodoscopes and the KL do not have a sufficient

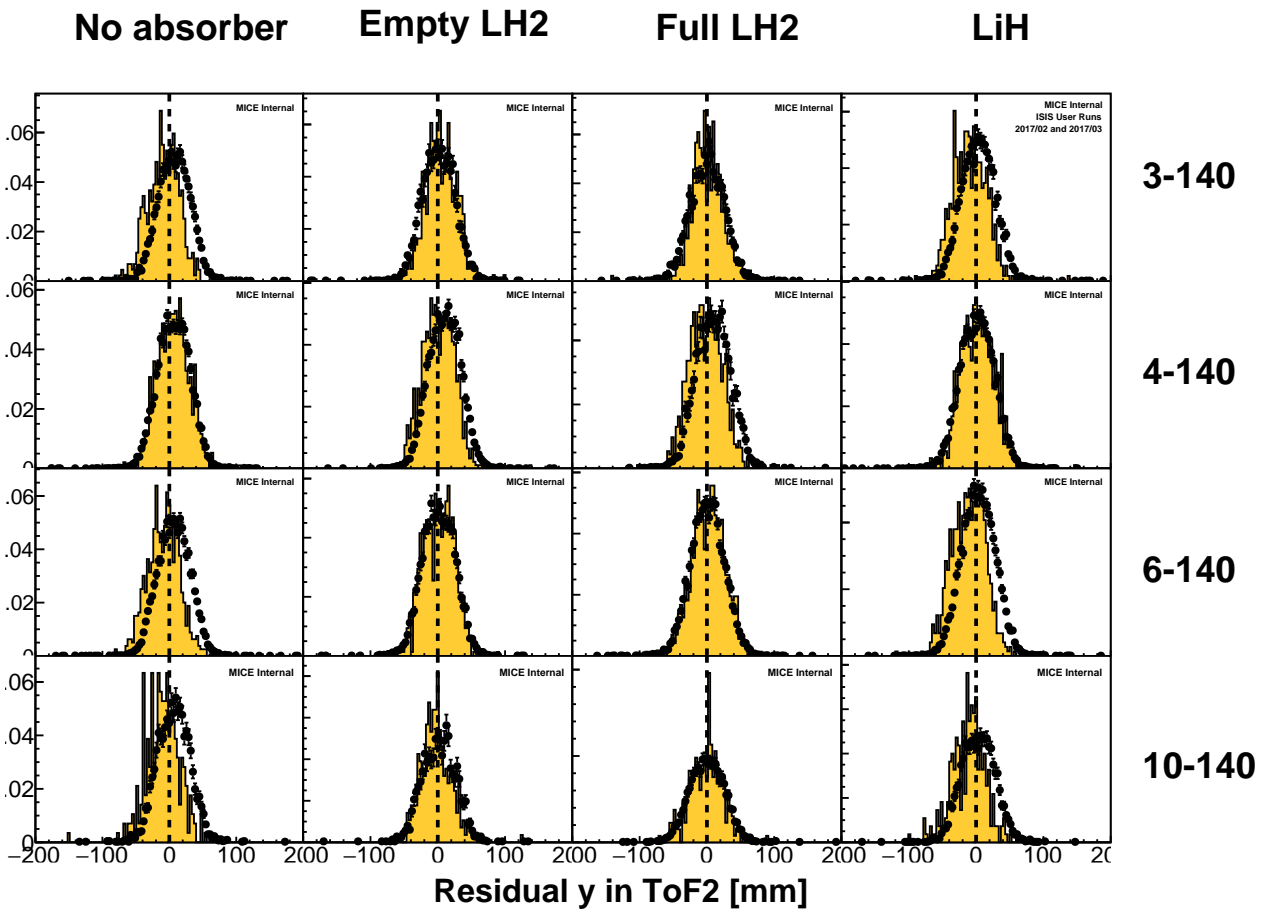


Figure 49: Residual  $y$  position of TKD tracks extrapolated to TOF2, as compared to the position measured in TOF2.

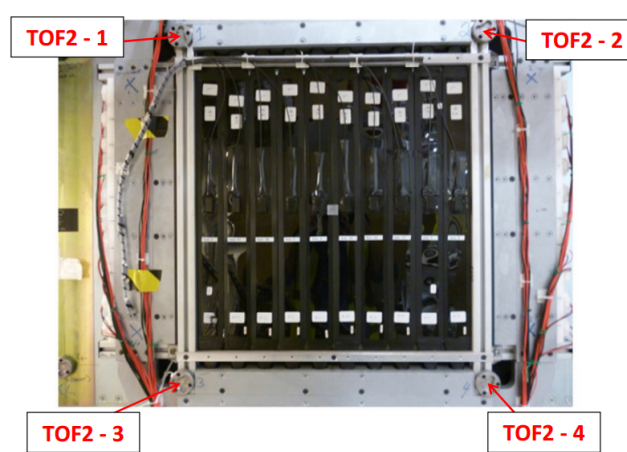


Figure 50: Picture of the TOF2 time-of-flight hodoscope and its four survey monuments labelled TOF2.1–2.4.

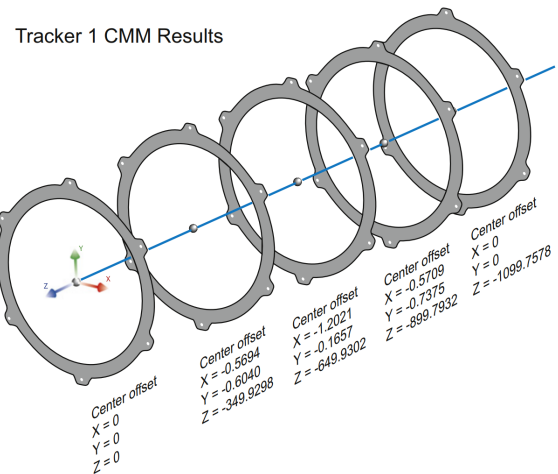


Figure 51: Disposition of the downstream tracker stations along with the CMM measurements of their position with respect to the reference axis.

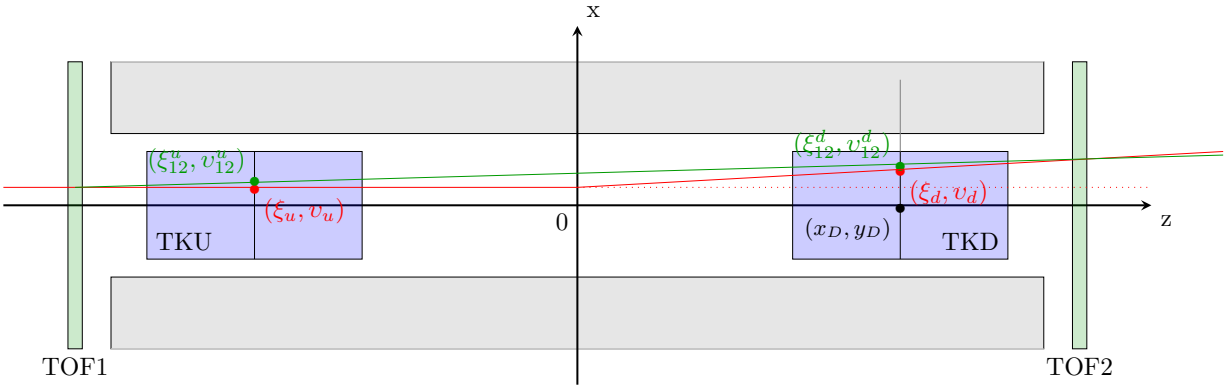


Figure 52: True path of a single particle track (red) and its path as reconstructed from the time-of-flight system (green). The position of the track at the tracker centres is represented by markers.

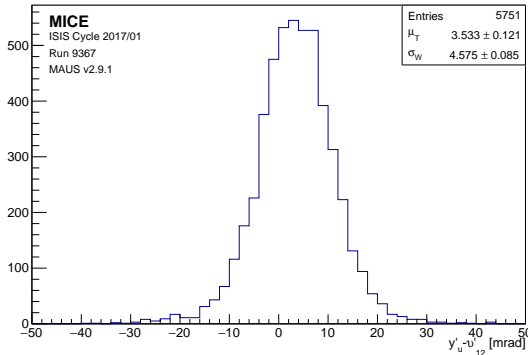


Figure 53: Residuals distribution between the pitch gradients measured locally in TKU,  $y'_u$ , and globally between TOF1 and TOF2,  $v'_{12}$ .

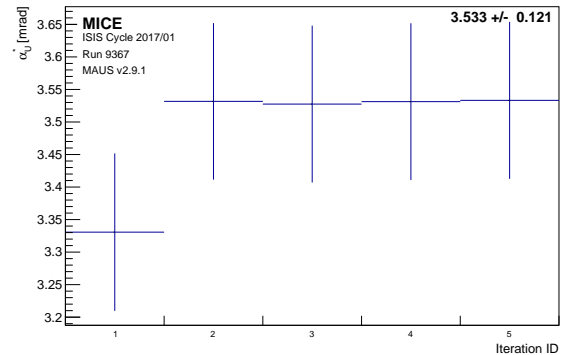


Figure 54: Evolution of the optimal value of the pitch angle in TKU,  $\alpha_U^*$ , for different number of iterations of the fitting algorithm.

resolution to produce residuals that follow a Gaussian distribution. A probability density function of the form

$$h(x) = \frac{1}{4W} \left( \tanh \left[ \frac{x - \mu + W}{\sigma} \right] - \tanh \left[ \frac{x - \mu - W}{\sigma} \right] \right) \quad (18)$$

is used in each projection to fit the residuals involving the low granularity detectors. The constant  $\mu$  represents the central value of the residual distribution,  $\sigma$  the residual width and  $W$  the half-width of one of the low-resolution detector pixel. The parameters obtained for each of the fits are represented on the residual graphs. The values found for  $W$  are consistent with pixels of 6 cm in TOF1 and TOF2 and of 4.4 cm in the KL.

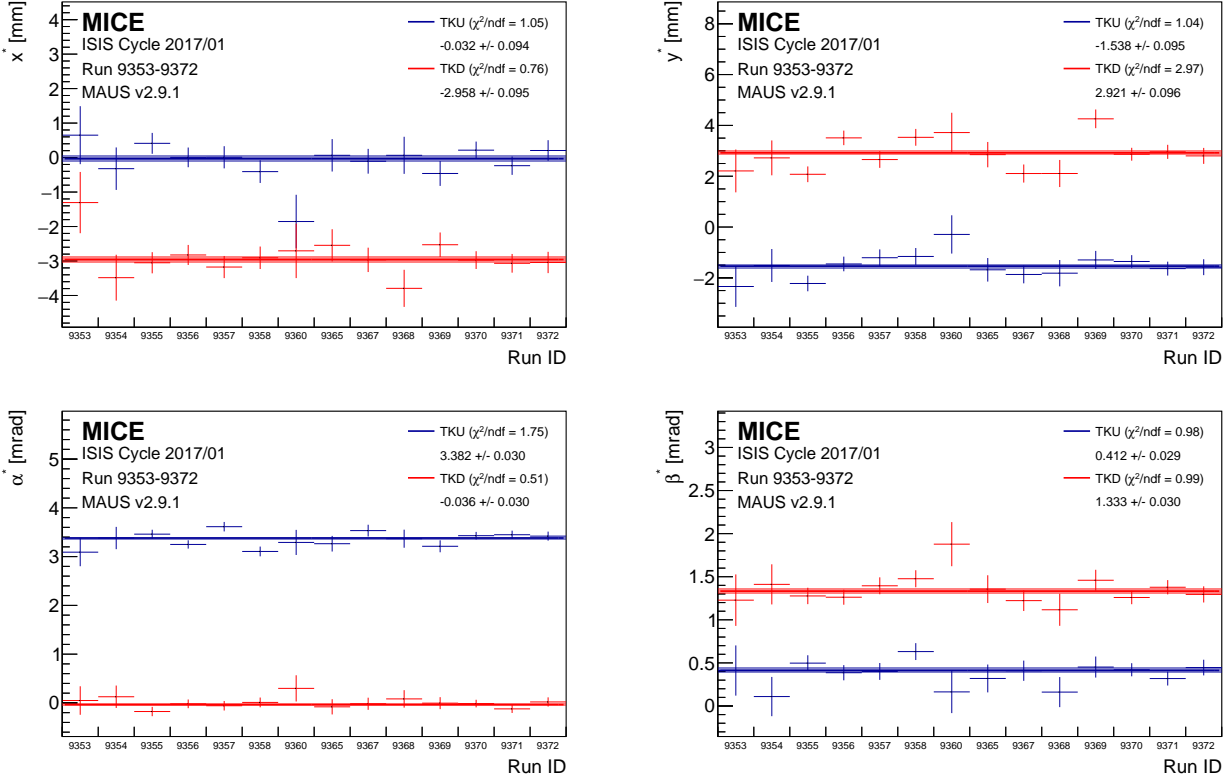


Figure 55: Consistency of the alignment algorithm across runs acquired during the 2017/01 ISIS user cycle.

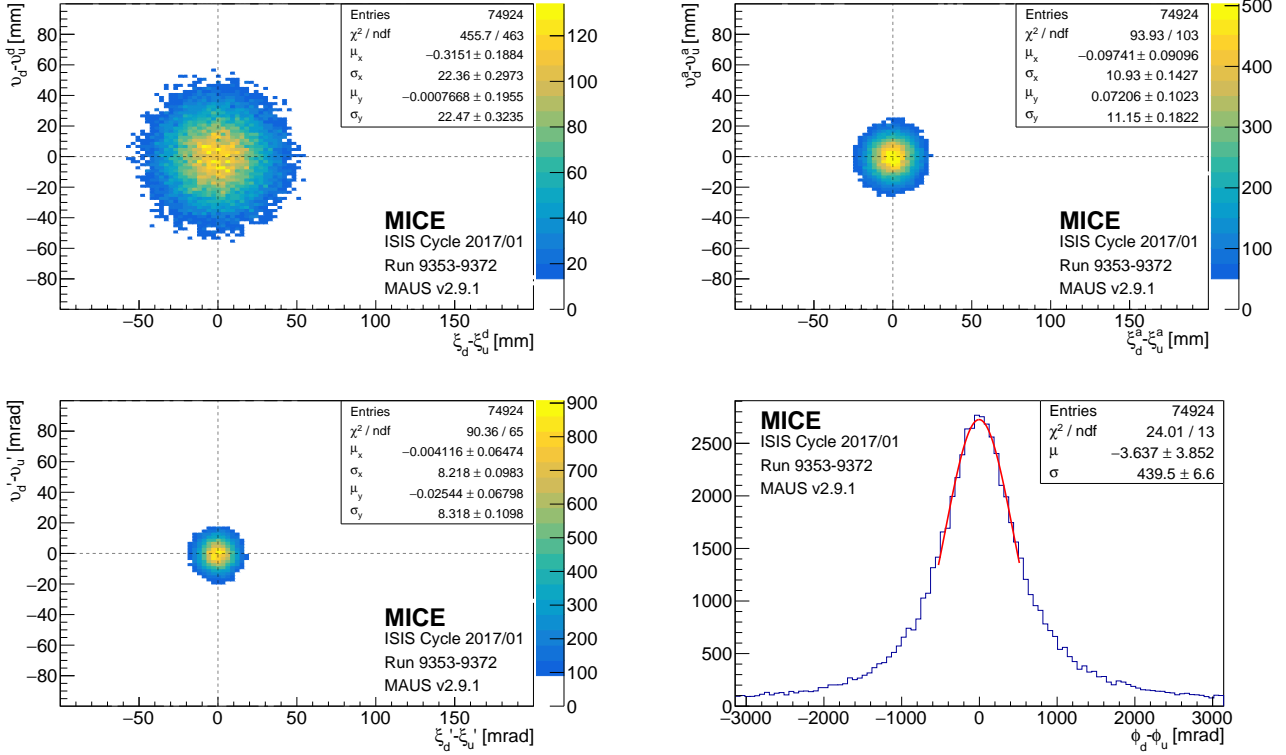


Figure 56: Tracker-to-tracker residual distributions in position (**top**) and angle (**bottom**).

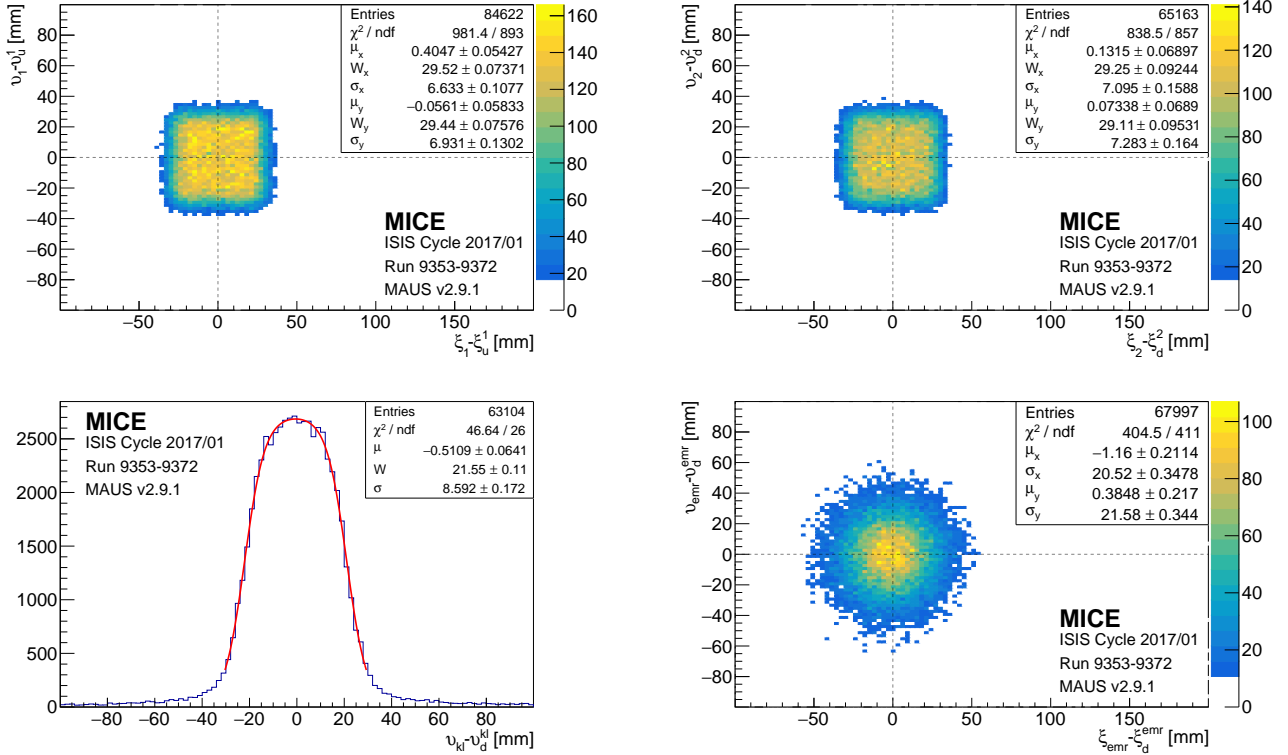


Figure 57: Tracker to particle identification detectors residual distributions (TOF1, TOF2, KL and EMR).

## 630 10 Magnets and Beam Optics

### 10.1 Introduction

### 10.2 Beam based magnet alignment

### 10.3 Beam line optics

## 11 Absorber

635 As a muon beam passes through material, some of the kinetic energy of the muons is lost through ionization of the material. This process results in a reduction of the normalised transverse emittance and the beam is said to be cooled. Muons will also undergo multiple Coulomb scattering which increases the divergence of the beam, thereby increasing the normalised transverse emittance and heating the beam.

640 Ionization-energy loss is characterised by  $\frac{dE}{dx}$ , where  $E$  is the muon energy and  $x$  is the distance travelled within the absorber. Multiple Coulomb scattering is characterised by the radiation length,  $X_0$ . For liquid hydrogen,  $\frac{dE}{dx} \sim 0.03 \text{ MeV/mm}$  and  $X_0 \sim 8905 \text{ mm}$  [? ]. The absorber vessel was manufactured using aluminium for which  $\frac{dE}{dx} \sim 0.4 \text{ MeV/mm}$  and  $X_0 \sim 90 \text{ mm}$  [? ]. To maximise the cooling effect from energy loss in liquid hydrogen, while minimising the heating effect from multiple Coulomb scattering in the aluminium windows, these windows were required to be as thin as possible.

645 Figure ?? shows the drawings of the absorber focus coil (AFC) module and the installed absorber vessel. The absorber vessel was set at the centre of the FC magnet coils. Safety considerations required a secondary containment system. Therefore, the absorber vessel was situated in an evacuated space within two more thin

aluminium safety windows, so the muon beam had to traverse four windows, as shown in the left panel in Figure ??.

650 geometry definition and validation.

## 11.1 Absorber vessel body

The absorber vessel comprised a cylindrical aluminium body sealed with two thin aluminium end windows, as shown in the right panel of figure ?? . The absorber vessel was specified to contain  $22\text{ l}$  of liquid, so the body had an inner diameter of 300 mm and a length between its end flanges of 230 mm. The length along the central axis between the two domes of the thin aluminium end windows was 350 mm. The body contained an annular cooling channel within its walls that could act as a heat exchanger. This channel was designed to allow the possibility of cooling the vessel body directly using liquid nitrogen, or even liquid helium. However, it was found that this cooling was not necessary because the absorber vessel cooled sufficiently quickly with cold gas from the condenser, as described in section ?? . Small indium-sealed flanges connected the aluminium pipes from the absorber vessel to the stainless-steel pipes from the condenser.

Figure 58 shows a photograph of the inside of the absorber vessel body. The two flanged windows were sealed to the end flanges of this body using indium contained in grooves. The heat exchanger fins and five pairs of thermometers (LakeShore Cernox 1050-SD) are visible in this photograph. These five thermometer pairs were inside the vessel at locations spaced by  $45^\circ$  around the circumference and were monitored with a LakeShore 218S. Each pair monitored the presence of liquid hydrogen at that position; one of these Cernox sensors was operated with a small current as a thermometer, and the other was occasionally heated by a pulse of larger current. The difference between the two measured temperatures was small when these sensors were in liquid due to good cooling efficiency, but the difference was larger when these sensors were in gas since heat transport through the gas is worse than in the liquid. The sensor wires were extracted to vacuum part-way along the liquid-hydrogen inlet pipe at a 30-pin hermetic feed-through, as shown in figure ?? . Signals from each sensor were carried on two wires inside the absorber vessel, between the sensor and the feed-through, and by four wires in the vacuum outside the vessel. Two Cernox thermometers and two heaters (LakeShore HR-25-100) were mounted externally on each end flange. Two additional Cernox thermometers were mounted externally on the hydrogen inlet and outlet lines. These thermometers were exposed to vacuum and thermal radiation so the thermometry here was less accurate than that inside the absorber vessel, but gave indications of the flow of cooling gas in the circuit. To minimise heat input from contact with the magnet bore, the absorber vessel was mounted on glass-epoxy (G10) supports of low thermal conductivity. To minimise radiative heat input, multilayer insulation (MLI) was wrapped around the absorber vessel and all the low-temperature pipework. The number of layers of MLI over the end windows was first entered into a Monte Carlo program to check that the scattering of muons by the MLI was insignificant compared to that of the windows, before the vessel was integrated into the system and cooled.

## 11.2 Windows

The liquid hydrogen was contained between two aluminium windows, each having a thickness of  $180\text{ }\mu\text{m}$  at the centre and increasing to  $360\text{ }\mu\text{m}$  near the outer flange. Aluminium safety windows, each with a central thickness of  $210\text{ }\mu\text{m}$ , enclosed the absorber vessel in the magnet bore. Thin aluminium was chosen to minimise multiple scattering. Thinner windows lead to less scattering and more muon-beam cooling. Although a MICE window with a central thickness of  $125\text{ }\mu\text{m}$  had successfully been machined using alloy 6061-T651, it would not withstand enough pressure. The pressure in the absorber vessel reached 1500 mbar during typical

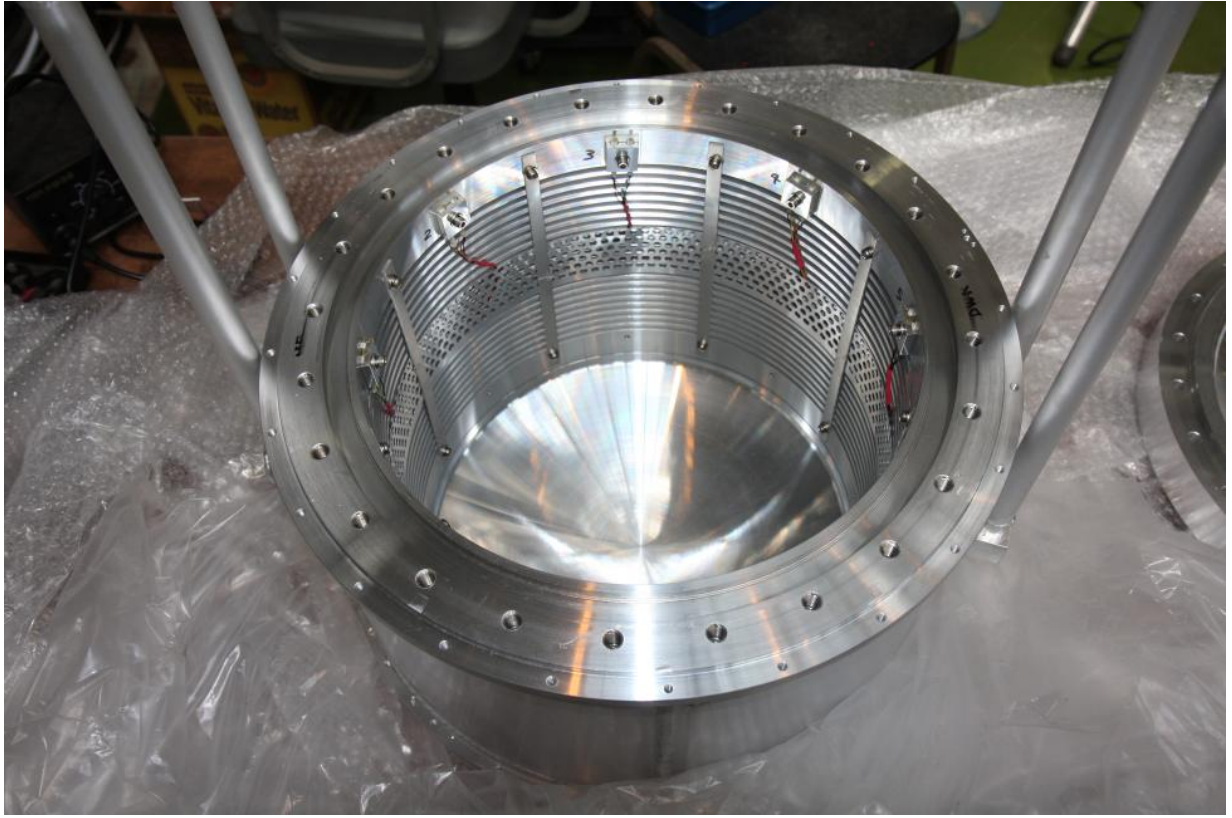


Figure 58: Photograph of the absorber vessel body.

operations. The aluminium alloy we chose to use (6061-T651) was assayed to contain 0.61% silicon, 0.26%  
690 iron, 0.25% copper, 0.02% manganese, 1.02% magnesium, 0.20% chromium, 0.01% zinc, 0.05% titanium,  
0.01% zirconium, 0.15% maximum other material, and at least 97.42% aluminium (all measured by weight).  
The yield strength was measured at room temperature to be  $39,900 \pm 700$  psi ( $275 \pm 5$  MPa), although this would  
be greater at 20 K. A drawing of a MICE absorber vessel window is shown in figure 59. The double-bend  
geometry increases the burst strength.

#### 695 11.2.1 Window manufacture

A CNC Fadal 5020A vertical machining centre and a CNC Romi lathe with a 27 inch swing were used to machine the windows from a solid block of aluminium alloy. Precision backing plates supported the windows during this process. Each window was machined to a  $2000 \mu\text{m}$  central thickness, and then measured with the micrometer jig shown in figure 62. The window was then returned to the lathe for final machining while the  
700 lathe still had the positions stored in its memory. Clear plastic cases were fabricated to protect the windows from damage in transit, while still allowing visual inspection. Finished windows can be seen in figures 60 and 63.

#### 11.2.2 Window thickness measurement

The thicknesses of three different types of finished windows (one absorber and two safety) were measured with  
705 the View Precis 3000 Optical Co-ordinates Measurement Machine (CMM) shown in figure 60. The complete

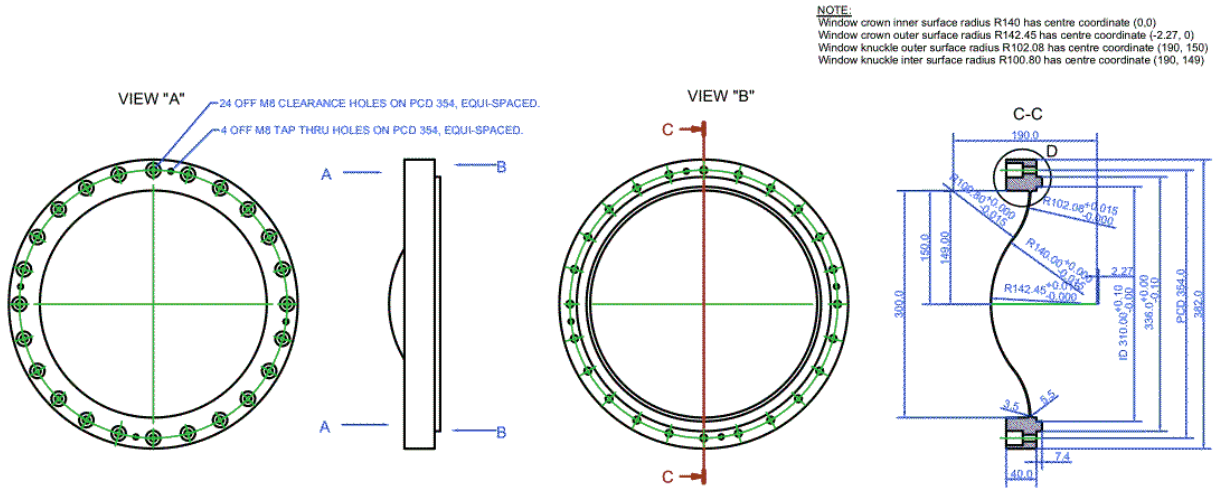


Figure 59: Aluminium absorber vessel window with a central thickness of  $180 \mu\text{m}$  for the containment of liquid hydrogen. Both types of safety windows were similar to the vessel window, but had a central design thickness of  $210 \mu\text{m}$ .

surface profile of a window was measured with the laser on one side, and then the window was turned over to measure the other side. The difference between the surface profiles of both sides of the window gave the thickness. Three tuning balls were glued to the window to establish the reference coordinate system; key to getting a good measurement was to establish the same reference coordinate system for both sides of each window. Some results of the measurements are shown in table 10 and figure 61. For some of the windows, the thickness measurement was checked by scanning only the small area around the window centre with a very dense meshing. This gave a more accurate measurement of the thickness at the window centre.

Low energy electrons are strongly attenuated by modest thicknesses of aluminium. Two different beta sources,  $^{90}\text{Sr}$  and  $^{204}\text{Tl}$ , were used to measure the thickness of a MICE window. The source and detector (Geiger tube) were on opposite sides of the window so there was no need to move the window during this process, as was required with the laser CMM. The attenuation of electrons in a thin sheet of material of thickness  $x$  was described using the equation:

$$R = A e^{\alpha x} + B e^{\beta x} + C. \quad (19)$$

The apparatus was optimised to measure the central window thickness by choosing beta sources with electron energies that have a half-range of about  $180 \mu\text{m}$  in aluminium. Due to electron scattering, the result can be sensitive to apparatus geometry so a careful calibration was performed using aluminium sheets of known thickness with counts being accumulated for 10 minutes per sheet. The central thickness of the absorber window in figure 63 was measured to be  $178 \pm 6$  (stat)  $\pm 4$  (fit)  $\mu\text{m}$ .

### 11.3 Validation of the absorber model in MAUS

### 11.4 refs

## 720 12 Conclusions

To be written at last.

Table 10: Results of measuring the central thickness of the three types of windows with the View Precis 3000 Optical CMM shown in figure 60. The windows actually used in MICE were numbers 002, 003, 009, and 014.

Window #	Window Type	Central Thickness Measured ( $\mu\text{m}$ )	Central Thickness Design ( $\mu\text{m}$ )	Note
001	Absorber		180	
002	Absorber	$174 \pm 5$	180	
003	Absorber	$184 \pm 2$	180	
004	Absorber		180	
005	Absorber	$176 \pm 6$	180	
006	Safety I	$222 \pm 6$	210	flaw at centre
007	Safety I		210	flaw at centre
008	Safety II	$233 \pm 5$	210	
009	Safety II	$230 \pm 9$	210	
010	Absorber		180	
011	Absorber		180	
012	Safety I	$197 \pm 7$	210	
013	Safety I		210	
014	Safety I	$197 \pm 8$	210	



Figure 60: The View Precis 3000 Optical CMM measured the surface profile of each window, one side at a time.



Figure 61: Result of the CMM measurement of one side of one window. All the axes are labelled in units of millimetres.



Figure 62: Jig for measuring window thickness at the centre and at  $15^\circ$  from the peak of the dome with a pair of Starrett T465 micrometers accurate to 3 microns.



Figure 63:  $^{90}\text{Sr}$  and  $^{204}\text{Tl}$  beta sources and a Geiger tube were used to check the central thicknesses of windows.



Figure 64: This absorber vessel window burst when pressurised with water.



Figure 65: This Type I safety window (number 012 in Table 10) burst when slowly pressurised with nitrogen gas.

## References

- [1] M. Bonesini, “The design of MICE TOF0 detector,” *MICE Note 145* (2006) .  
<http://mice.iit.edu/micenotes/public/pdf/MICE0145/MICE0145.pdf>.
- 725 [2] R. Bertoni *et al.*, “The construction and laboratory tests for MICE TOF0/1 detectors,” *MICE Note 241* (2008) . <http://mice.iit.edu/micenotes/public/pdf/MICE0241/MICE0241.pdf>.
- [3] R. Bertoni, A. Blondel, M. Bonesini, G. Cecchet, A. de Bari, J. S. Graulich, Y. Karadzhov, M. Rayner, I. Rusinov, R. Tsenev, S. Terzo, and V. Verguilov, “The design and commissioning of the MICE upstream time-of-flight system,” *Nuclear Instruments and Methods in Physics Research A* **615** (Mar., 2010) 14–26, arXiv:1001.4426 [physics.ins-det].
- 730 [4] R. Bertoni *et al.*, “The construction of the MICE TOF2 detector,” *MICE Note 286* (2010) .  
<http://mice.iit.edu/micenotes/public/pdf/MICE0286/MICE0286.pdf>.
- [5] D. Rajaram and V. C. Palladino, “The Status of MICE Step IV,”.  
<http://accelconf.web.cern.ch/AccelConf/IPAC2015/papers/thpf122.pdf>.
- 735 [6] M. Bonesini, “Progress of the MICE experiment,” arXiv:1510.08825 [physics.acc-ph].
- [7] The MICE Collaboration, “Characterisation of the muon beams for the Muon Ionisation Cooling Experiment,” *ArXiv e-prints* (June, 2013) , arXiv:1306.1509 [physics.acc-ph].
- [8] D. Adams *et al.*, “Pion contamination in the MICE muon beam,” *Journal of Instrumentation* **11** (Mar., 2016) P03001, arXiv:1511.00556 [physics.ins-det].
- 740 [9] Y. Karadzhov *et al.*, “TOF detectors Time Calibration,” *MICE Note 251* (2009) .  
<http://mice.iit.edu/micenotes/public/pdf/MICE0251/MICE0251.pdf>.
- [10] M. Bonesini, R. Bertoni, A. de Bari, and M. Rossella, “Behaviour in magnetic fields of fast conventional and fine-mesh photomultipliers,” *Nuclear Instruments and Methods in Physics Research A* **693** (Nov., 2012) 130–137, arXiv:1207.4909 [physics.ins-det].
- 745 [11] M. Bonesini *et al.*, “The TOF1 local shielding,” *MICE Note 455* (2015) .  
<http://mice.iit.edu/micenotes/public/pdf/MICE0455/MICE0455.pdf>.
- [12] L. Cremaldi *et al.*, “Progress on Cherenkov Reconstruction in MICE,” *MICE Note 473* (2015) .  
<http://mice.iit.edu/micenotes/public/pdf/MICE0473/MICE0473.pdf>.
- 750 [13] R. Asfandiyarov *et al.*, “The design and construction of the MICE Electron-Muon Ranger,” *Journal of Instrumentation* **11** (Oct., 2016) T10007, arXiv:1607.04955 [physics.ins-det].
- [14] F. Drielsma, “Electron-Muon Ranger: hardware characterization,” Master’s thesis, University of Geneva, 2014. <https://arxiv.org/abs/1710.06946>.
- [15] D. Adams *et al.*, “Electron-muon ranger: performance in the MICE muon beam,” *Journal of Instrumentation* **10** (Dec., 2015) P12012, arXiv:1510.08306 [physics.ins-det].
- 755 [16] F. Drielsma, *Measurement of the Increase in Phase Space Density of a Muon Beam through Ionization Cooling*. PhD thesis, University of Geneva, 10, 2018.
- [17] F. Drielsma, “Beam-based detector alignment in the MICE muon beam line,” arXiv:1805.06623 [physics.ins-det]. <https://arxiv.org/abs/1805.06623>.